

MODELING THE PHYSICAL STRUCTURE OF THE LOW DENSITY PRE-PROTOSTELLAR CORE LYND 1498

YANCY L. SHIRLEY¹
 NRAO, P.O. Box O, Socorro, NM 87801
 yshirley@nrao.edu

MIRANDA K. NORDHAUS²
 Applied Physics and Astronomy, Rensselaer Polytechnic Institute, Troy, NY 12180
 nordhm@rpi.edu

JANA M. GRCEVICH³
 University of Wisconsin-Madison, Department of Astronomy, 475 North Charter Street, Madison, WI 53706
 jmgrcevich@students.wisc.edu

NEAL J. EVANS II
 Department of Astronomy, The University of Texas at Austin, Austin, Texas 78712-1083
 nje@astro.as.utexas.edu

JONATHAN M. C. RAWLINGS
 Department of Physics and Astronomy, University College London, Gower Street, London WC1E 6BT
 jcr@star.ucl.ac.uk

AND

KEN'ICHI TATEMATSU
 National Astronomical Observatory of Japan, 2-21-1 Osawa, Mitaka Tokyo 181-8588, Japan
 k.tatematsu@nao.ac.jp
Draft version November 5, 2018

ABSTRACT

Pre-protostellar cores likely represent the incipient stages of low-mass ($\approx 1M_{\odot}$) star formation. Lynds 1498 is a pre-protostellar core (PPC) and was one of the initial objects toward which molecular depletion and differentiation was detected. Despite the considerable scrutiny of L1498, there has not been an extensive study of the density and temperature structure as derived from radiative transfer modeling of dust continuum observations. We present deep SCUBA observations of L1498 at 850 and 450 μm , high resolution BEARS maps of the N_2H^+ $1 \rightarrow 0$ transition, CSO observations of the N_2H^+ $3 \rightarrow 2$ transition, and GBT observations of the C_3S $4 \rightarrow 3$ transition. We also present a comparison of derived properties between L1498 and nearby PPCs that have been observed at far-infrared and submillimeter wavelengths. The L1498 continuum emission is modeled using a one-dimensional radiative transfer code that self-consistently calculates the temperature distribution and calculates the SED and intensity profiles at 850 and 450 μm . We present a more realistic treatment of PPC heating which varies the strength of the ISRF, s_{isrf} , and includes attenuation of the ISRF due to dust grains at the outer radius of the core, A_V . The best-fitted model consists of a Bonner-Ebert sphere with a central density of $1 - 3 \times 10^4 \text{ cm}^{-3}$, $R_o \approx 0.29 \text{ pc}$, $0.5 \leq s_{\text{isrf}} \leq 1$, $A_V \approx 1 \text{ mag}$, and a nearly isothermal temperature profile of $\approx 10.5 \text{ K}$ for OH8 opacities. C_3S emission shows a central depletion hole while N_2H^+ emission is centrally peaked. We derive a mean N_2H^+ abundance of 4.0×10^{-10} relative to H_2 that is consistent with chemical models for a dynamically young yet chemically evolved source. The observed depletions of C_3S and H_2CO , the modest N_2H^+ abundance, and a central density that is an order of magnitude lower than other modeled PPCs suggests that L1498 may be a forming PPC. Our derived temperature and density profile will improve modeling of molecular line observations that will explicate the core's kinematical and chemical state.

1. INTRODUCTION

Pre-protostellar Cores (PPCs or starless cores) are thought to represent the initial stages of low-mass ($M < \text{few } M_{\odot}$) star formation. PPCs are identified with dense molecular cores ($n \geq 10^4 \text{ cm}^{-3}$) which lack evidence for an

internal heating source. Their column density is traced by dust continuum emission (Ward-Thompson et al. 1994; Ward-Thompson, Motte, & André 1999; Shirley et al. 2000; Tafalla et al. 2002) and nitrogen-bearing molecular tracers such as NH_3 and N_2H^+ (Myers & Benson 1983, Ji-

¹ Jansky Postdoctoral Fellow at the National Radio Astronomy Observatory. The National Radio Astronomy Observatory is a facility of the National Science Foundation operated under a cooperative agreement by Associated Universities, Inc.

² 2003 REU Summer Student at NRAO Socorro.

³ 2004 REU Summer Student at NRAO Socorro.

jina et al. 1999, Caselli et al. 2002, Crapsi et al. 2005). It is important to characterize their physical structure (density, temperature, kinematical, and chemical) to constrain the initial conditions of low-mass star formation. It is also important to understand the evolution of the physical structure of PPCs to trace the evolution of a nascent protostar.

Lynds 1498 is a nearby molecular core ($D = 140$ pc) located in the west-central portion of the Taurus molecular cloud (see Cambr  sy 1999). L1498 was classified as a Pre-protostellar core by its submillimeter dust emission and lack of an IRAS detection at $100 \mu\text{m}$ (Ward Thompson et al. 1994). The relatively weak submillimeter dust emission indicated that L1498 was a low density core.

L1498 has been extensively studied with molecular line observations and using theoretical chemical modeling (Rawlings et al 1992, Taylor et al 1996). L1498 was initially identified kinematically as a core potentially on the verge of protostellar collapse (Zhou et al. 1994). Subsequent molecular line observations have shown dramatic evidence for the freezing of gas phase molecules onto dust grains (e.g., H_2CO , CS, CCS, C^{18}O ; Wang 1994; Lemme et al. 1995; Kuiper, Langer, & Velusamy 1996; Willacy, Langer, & Velusamy 1998, Tafalla et al. 2004); as a result, many molecular species cannot reliably trace the densities in the center of the core. Prominent exceptions are the nitrogen-bearing molecules NH_3 and N_2H^+ which resist depletion (Flower, Pineau des For  ts, & Walmsley 2005). Even though NH_3 and N_2H^+ remain in the gas phase in cold, dense molecular cores, the optical depth, gas temperature, and abundance profile must be reliably determined in order to accurately calculate the density structure of the core.

Optically thin dust emission at submillimeter wavelengths is a good tracer of temperature and density since the specific intensity is proportional to the integral of density, opacity, and Planck function along a line-of-sight

$$I_\nu = \frac{2\mu m_{\text{H}} h \nu^3}{c^2} \int_0^\infty \frac{\kappa_\nu(s) n(s)}{\exp\left(\frac{h\nu}{kT_d(s)}\right) - 1} ds \quad (1)$$

(Adams 1991, Shirley et al. 2003). Knowledge of the temperature and density structure is essential to a correct interpretation of chemical and kinematic models of L1498. Previous dust continuum studies of PPCs used radiative transfer models to constrain the density and temperature structure of the cores (e.g. Evans et al. 2001, Zucconi et al. 2001, Stamatellos & Whitworth 2004). The density structures are well characterized by Bonner-Ebert spheres (hereafter, BE): pressure bounded, isothermal solutions to the equations of hydrostatic equilibrium that do not include the effects of magnetic fields or turbulence. A general picture of the initial stages of low-mass star formation involves the evolution of a BE sphere from low central density to high central density, perhaps retarded by magnetic pressure, until a central hydrostatic core develops. If we wish to understand the beginning of this process, we must identify and study low density PPCs.

In this paper we present deep submillimeter maps of L1498 (§2.1) with radiative transfer modeling which includes a more sophisticated treatment of the heating of the PPC (§3). The results of dust continuum modeling are discussed in §4. A comparison between the derived

properties from dust continuum observations of PPCs that were observed with ISO and SCUBA is discussed in §4.1.2. We also present the highest resolution single-dish N_2H^+ and C_3S maps of L1498 (§2.2, §2.3) with analysis of variations in the column density, abundance, and velocity (§4.2, §4.3).

2. OBSERVATIONS

2.1. SCUBA Continuum Observations

2.1.1. Reduction

L1498 was observed simultaneously at 850 and 450 μm with SCUBA on the 15 m James Clerk Maxwell Telescope during the nights of August 29 and 30, 1998. A total of fifty jiggle maps were made towards the source, each map consisting of four 64-point jiggle maps with 256s of ON-source integration time. The total ON-source integration time was 3.55 hours. Previous spectral line maps showed that L1498 is extended in a SE to NW direction; therefore, the chop angle was set to a constant position angle of 20° with a $120''$ chop throw to chop perpendicular to the major axis of the core. Non-azimuthal chopping results in a slight reduction in signal-to-noise in the map since a symmetrical chopping pattern does not lie at constant airmass. A preliminary map made in April, 1998 showed that the source was detected to the edge of a single 64-point jiggle map field-of-view ($2.3'$). Therefore, the map was extended using three offset 5-pointing maps, each with $30''$ spacing (see Figure 1a). The five-pointing maps were centered at $(0'', 0'')$, $(+30'', -30'')$, and $(-30'', +30'')$ from the central coordinates of J2000.0 $\alpha = 4^{\text{h}} 10^{\text{m}} 52.5^{\text{s}}$, $\delta = +25^\circ 9' 55''$. The final maps spans $\pm 140''$ in right ascension and declination.

Each map was reduced using the standard SURF (SCUBA User Reduction Facility) reduction routines (Jenness & Lightfoot 1997). Each 64-point jiggle map was flat-fielded and corrected for chop throw, extinction, and sky noise. The 450 μm images were reduced using a set intensity scale to ensure consistent identification of improper sky noise subtraction. The telescope pointing was checked every hour. The largest pointing shift was $2.5''$; therefore, the standard pointing offsets from the five-pointing maps were used to shift and add together the individual maps.

Skydips at 850 μm and 450 μm were performed every hour during both nights. These skydips are compared to the opacity measured every 10 minutes at 225 GHz (τ_{CSO}) and 350 μm from tippers located at the Caltech Submillimeter Observatory. The τ_{CSO} data was only available for the night of August 30. Using the relationship derived by Archibald et al. (2002) between τ_{CSO} and the skydip-determined opacity at 850 μm (τ_{850}), $\tau_{850} = (3.99 \pm 0.02)(\tau_{\text{CSO}} - 0.004 \pm 0.001)$, we found excellent agreement between our skydips and the scaled 850 μm opacity (Figure 2). Therefore, we use the scaled τ_{CSO} values to correct for the 850 μm opacity in individual jiggle maps on the night of August 30. We linearly interpolated between 850 μm skydips for the night of August 29.

Since the sky opacity at 350 μm and 450 μm is very sensitive to short term variations in atmospheric precipitable water vapor, we used the tipper opacity at 350 μm to monitor the variability of τ_{450} between the hourly sky-

dips. We found an average ratio of τ_{450} skydips to τ_{350} of 0.71 ± 0.07 for both nights. The $450 \mu\text{m}$ opacity was corrected for each jiggle map using the scaled τ_{350} opacity interpolated from the tipper measurements bracketing each jiggle map.

2.1.2. Images

The reduced maps are shown in Figure 1. L1498 was detected at both wavelengths with a peak signal-to-noise of 18 and 13 for the $850 \mu\text{m}$ and $450 \mu\text{m}$ maps, respectively. The contours are spaced by 3σ for both images. The sub-millimeter images are characterized by an amazingly flat intensity plateau. A $1200 \mu\text{m}$ continuum map, smoothed to $20''$ resolution (Tafalla et al. 2004), is also shown for comparison. The FWHM intensity contour of the 1200 , 850 , and $450 \mu\text{m}$ maps are very similar and well fitted by an ellipse with a major axis (a) of $197''$, minor axis (b) of $108''$, and position angle of 122° . The $850 \mu\text{m}$ and $450 \mu\text{m}$ ellipses have similar centroids ($+11''$, $-16''$) with an uncertainty of $\pm 4''$ with respect to the pointing center (§2.1.1). The HWHM radius of the core, defined by the geometric mean of the major and minor axes ($R_{1/2} = \sqrt{ab}/2$), is $73''$. While this radius may be used as a representative size of the core, it is important to realize that the FWHM contour is asymmetric with an aspect ratio (a/b) of 1.8. Furthermore, the $1200 \mu\text{m}$ and $850 \mu\text{m}$ maps are non-axisymmetric with a sharper gradient in the intensity along the northeast edge compared to the southwest edge.

The ISO map at $170 \mu\text{m}$ is also shown in Figure 1b (Ward-Thompson et al. 2002). This is the shortest wavelength at which the far-infrared emission has been observed to peak on the core; ISO $90 \mu\text{m}$ observations detect a more diffuse emission peak approximately $3'$ south of the submillimeter centroid. The scale of the $170 \mu\text{m}$ map is $\pm 300''$, twice the scale in the (sub)-millimeter maps. The ISO beam was very large ($\approx 80''$) at $170 \mu\text{m}$; therefore, the map does not show the non-axisymmetric structure observed on smaller scales at 850 and $1200 \mu\text{m}$. The core is elongated, but with a slightly different position angle on larger scales ($\text{PA} \sim 150^\circ$). Far-infrared emission is detected on very large scales, up to $300''$ ($42,000 \text{ AU}$) from the centroid of the submillimeter emission.

Azimuthally-averaged, normalized radial profiles of the 850 , 450 , and $1200 \mu\text{m}$ maps were calculated. The images were re-binned to pixels with half beam spacing ($7''$ at $850 \mu\text{m}$ and $3.5''$ at $450 \mu\text{m}$) corresponding to the Nyquist sampling limit in the map. The centroid was chosen to be the average of the 850 and $450 \mu\text{m}$ centroids ($+11''$, $-16''$). The $1200 \mu\text{m}$ profile was binned at $10''$ since the image was smoothed by a $20''$ Gaussian (Tafalla et al. 2004). The flat intensity plateau has the same extent in all of the profiles.

Since L1498 is a very elongated core, azimuthally averaged profiles will be weighted towards a flatter intensity profile (see Jørgensen et al. 2002). This effect may be quantified by considering the normalized profile within sectors centered on the major and minor axes. If the sector centered on the major axis is chosen with the opening angle given by,

$$\theta_{\text{maj}} = 2 \tan^{-1}(b/a), \quad (2)$$

where b/a is the ratio of the minor to major axes ($\theta_{\text{min}} + \theta_{\text{maj}} = \pi$), then the areas of sectors are equal. The

azimuthally averaged and sector-averaged profile will be modeled separately in §3.

2.1.3. Calibration and the SED

Uranus and AFGL618 were observed on August 29 and 30 as flux calibrators and for beam profiles at 850 and $450 \mu\text{m}$. The total flux of Uranus was 74.0 Jy at $850 \mu\text{m}$ and 195.5 Jy at $450 \mu\text{m}$. The apparent diameter of Uranus was $3''.7$ effectively making Uranus a point source at both wavelengths (see Shirley et al. 2000 for an analysis of Uranus' finite size on the beam size). The flux of AFGL618 was assumed to be $4.56 \pm 0.17 \text{ Jy/beam}$ at $850 \mu\text{m}$ and $11.2 \pm 1.4 \text{ Jy/beam}$ at $450 \mu\text{m}$ (SCUBA Secondary Calibrator Webpage⁴). Since we are interested in the total flux observed towards L1498, we calibrated the flux in apertures of $40''$ and $120''$. Flux densities are calculated for an aperture diameter, θ , using $S_\nu(\lambda, \theta) = C(\lambda, \theta)V(\lambda, \theta)e^{-\tau \sec z}$, where $V(\lambda, \theta)$ was the voltage measured at wavelength λ in an aperture of diameter θ at airmass $\sec z$ and $C(\lambda, \theta)$ is the calibration factor. The fluxes for L1498 are included in the source properties in Table 1. The uncertainty on the calibration factor was calculated by propagating the errors using,

$$\sigma_{S_\nu}^2 = S_\nu^2 \left[\left(\frac{\sigma_C^2}{C^2} \right)_{\text{Run Avg}} + (\sec^2 z \sigma_\tau^2)_{\text{Source}} + \frac{\Sigma_{\text{pixels}} A_i^2 \sigma_{V_i}^2}{C^2 V^2} \right] \quad (3)$$

where S_ν is the flux density (Jy), C is the calibration factor (Jy/V), V is the total voltage observed within the aperture (V), and A_i is the area of a pixel included within the aperture.

The SCUBA beam profiles were determined using observations of Uranus at 850 and $450 \mu\text{m}$. Uranus was observable only at the beginning of our observing shift and only at high airmass ($\sec z \sim 2$). The Uranus profile cannot be traced beyond $60''$ at $850 \mu\text{m}$ and beyond $50''$ at $450 \mu\text{m}$. Unfortunately, AFGL618 is not strong enough to be used for extended beam profiles ($\theta > 25''$). The Uranus profiles are very similar to the average Uranus beam profile determined from maps made in April, 1998 (Shirley et al. 2000). Since all of our observation were made during the morning observing shift (1:30AM HST - 9:30AM HST), the dish should have cooled sufficiently such that the beam shape is stable. No significant trends were seen in the April 1998 beam maps observed during the morning observing shift; therefore, we feel justified in using the Uranus beam profile for all second shift observations.

The SED was constructed from our SCUBA observations and a search of the literature (Table 1). The SED includes previous (sub)-millimeter observations by Ward-Thompson et al. (1994) as well as ISO far-infrared observations at 170 and $200 \mu\text{m}$ (Ward-Thompson et al. 2002). The inclusion of the far-infrared fluxes is extremely important for bracketing the peak of the SED.

2.2. N_2H^+ Observations

2.2.1. BEARS

Lynds 1498 was mapped with BEARS, a 25-beam double-sideband SIS receiver array that operates at 3mm (Sunada et al. 2000), on April 26, 2004 at the Nobeyama

⁴ www.jach.hawaii.edu/JACpublic/JCMT/Continuumobserving/SCUBA/astronomy/calibration/secondary2004.html

Radio Observatory 45 m telescope. The average beam-size within the array is $17''.8$ at 93.17 GHz (Tatematsu et al. 2004); however, each beam in the array is separated by slightly more than $2\theta_{\text{fwhm}}$ ($41''.1$). We observed the source using a dithered 4×4 position-switched grid on the sky spaced by $20''.55$. The array was rotated by $\pm 90^\circ$ after each dithered map to change relative beam positions with respect to the source. A digital autocorrelator backend with 37.8 kHz resolution (≈ 0.12 km/s) was used. BEARS was tuned to the frequency of the strongest hyperfine component (93.1737767 GHz $JF_1F = 123 \rightarrow 012$, see Appendix A). The resulting N_2H^+ map has 100 spectra separated at nearly full beam resolution and represents the highest resolution N_2H^+ spectrum obtained towards L1498.

BEARS tuning was consistent across the array with an average T_{sys} of 220 K. The intensity was calibrated for the receiver sideband ratio by observing the bright high-mass star-forming core, G40.50+2.54, with every beam in the BEARS array and the Nobeyama facility single-sideband S100 receiver. Spectra from the S100 receiver were calibrated on the T_A^* scale using the standard chopper-wheel method (Penzias & Burrus 1973). The calibration source was observed twice with the array rotated by 90° to minimize systematic calibration errors. The resulting calibration is good to approximately 20%. The spectra were converted to the T_R^* scale by assuming the BEARS sidelobes are negligible and using $\eta_{\text{mb}} = 0.51$ (Tatematsu et al. 2004).

Pointing observations were performed every hour using the $\text{SiO } v = 1, J = 1 \rightarrow 0$ maser transition towards NML Tau. The largest pointing shifts were $6''$ with average corrections of $4''$ and $3''$ in azimuth and elevation respectively. The weather was clear with winds typically below 6 m/s during L1498 observations. Conditions were good for N_2H^+ observations and the absolute pointing errors are small compared to the BEARS beamsize.

The data were baselined, summed, calibrated, and interpolated onto a regular spatial grid using the *NewStar*⁵ software package of the Nobeyama Radio Observatory. The reduced maps were written out to the group FITS format (Greisen & Harten 1981) and read into *AIPS++*. Fitting of the hyperfine components were performed with *Glish* scripts in *AIPS++*. The group FITS data cube was also written to a series of ASCII files for calculation of baseline rms and the integrated intensity.

2.2.2. CSO Observations

The $\text{N}_2\text{H}^+ J = 3 \rightarrow 2$ transition was observed in position-switched mode towards the centroid continuum position of Lynds 1498 with the Caltech Submillimeter Observatory on the night of July 24, 2004. The 230 GHz double sideband SIS receiver (Kooi 1992) with a 50 MHz AOS backend were used. The average T_{sys} was approximately 430 K. The spectral resolution was 147 kHz (0.15 km/s) after smoothing to the actual resolution of the spectrometer (3 channels). The receiver was tuned to the JPL line catalog frequency, 279.511701 GHz, for $\text{N}_2\text{H}^+ J = 3 \rightarrow 2$; this frequency is within 160 kHz of a blend containing the strongest hyperfine component (279.5118631 GHz, $JF_1F = 345 \rightarrow 234$; Luca Dore, priv. comm.).

Pointing and main beam calibration were performed on Venus. The main beam efficiency was determined to be $\eta_{\text{mb}} = 0.60 \pm 0.06$ at 279 GHz for a $26''.8$ beam. The pointing was consistent with a largest pointing shift of less than $3''$ in both azimuth and zenith angle during the observations. The spectra were smoothed, baselined, and summed using the *CLASS* software package (Buisson et al. 2002). L1498 was observed for a total of 10 minutes ON-source. The final spectrum has a baseline rms of $\sigma(T_R^*) = 45$ mK.

2.3. C₃S Observations

The $\text{C}_3\text{S } J = 4 \rightarrow 3$ transition at 23.1229820 GHz⁶ was mapped using the 100m Robert C. Byrd Green Bank Telescope on the nights of March 14 and 15, 2005. The spectrometer was setup to observe 4 IFs with 2 polarizations at 6.125 kHz resolution (0.079 km/s) using a single beam of the K-band receiver. The four IFs were centered on the $\text{C}_3\text{S } \text{C}_3^{34}\text{S}$, $^{13}\text{CCCS}$, and $\text{C}^{13}\text{CCS } J = 4 \rightarrow 3$ transitions. The observations were frequency switched by +4 MHz at a frequency of 4 Hz. Initially, a pointed map was made using a 7×5 grid, with 60s integration time per pointing, spaced at $33''$ (full beam spacing) centered on the SCUBA dust continuum centroid position. Three smaller 3×3 maps with $16''.5$ spacing were centered at the offsets (0,0), $(+49''.5, -16''.5)$, and $(-49''.5, +16''.5)$ with respect to the dust continuum centroid.

The raw frequency-switched spectra were folded and calibrated on the T_A scale using the *DISH* software package within *AIPS++*. The data were then written to ASCII files where opacity corrections were applied (T_A') and RR and LL polarizations were summed with $1/\sigma_{\text{baseline}}^2$ weighting. The opacity at 23.1 GHz was determined using the weather model of R. Maddalena (private communication) which averages the precipitable H_2O measurements from three nearby towns (Elkins, Hot Springs, and Lewisburg, West Virginia). The average zenith opacity was $\tau_{23.1} = 0.049 \pm 0.002$ on March 14 and $\tau_{22.5} = 0.106 \pm 0.002$ on March 15 during the observations. Final conversion to the T_{mb} scale was achieved using position-switched scans of the quasars 3C48 and 3C286. Unfortunately, the aperture efficiency was not properly determined at 23.1 GHz on March 14; therefore, we have linearly interpolated from measurements made at 9 GHz (Langston et al. 2004) and 46 GHz (March 18, 2005) to find $\eta_a = 0.54 \pm 0.11$. The GBT has an active surface which mitigates variations in the aperture efficiency with elevation and temperature. We have applied a 20% systematic uncertainty to account for these effects. The main beam efficiency is then $\eta_{\text{mb}} = 0.74 \pm 0.15$. The T_{mb} temperature scale may be compared with observations on the T_R^* scale if the sidelobe pickup is negligible (see Chapter 8.2.5 of Rohlfs & Wilson 2000); this is a reasonable assumption for the K-band receiver on the GBT.

Pointing and focusing were performed once per hour. The sky was clear and the wind was less than 4 m/s on both March 14 and March 15 during the observations. Since the observations were performed at nighttime, the temperature variation was small ($\Delta T < 1.9^\circ\text{C}$). The pointing and focus were very stable with a largest pointing shift

⁵ <http://www.nro.ac.jp/nro45mrt/NEW45m/NewStar/index.html>

⁶ Frequencies for transitions of C_3S and its isotopologues are from The Cologne Database for Molecular Spectroscopy (Müller et al. 2001): <http://www.ph1.uni-koeln.de/vorhersagen/>

of $7''$.

3. MODELS

3.1. 1D Continuum Radiative Transfer

The dust continuum observations are modeled using the one-dimensional radiative transfer code *CSDUST3* (Egan, Leung, & Spagna 1988) that self-consistently calculates the temperature distribution for a given density distribution, dust opacity, and ISRF. *CSDUST3* simulates anisotropic scattering which may affect the temperature distribution in the outer regions of the core, a feature that is not present in the radiative transfer code of Ivezić, Nenkova, & Elitzur (1999). Once the temperature distribution has been calculated, the intensity profiles at 850 and 450 μm are created by convolving the model intensity profiles with the measured beamshape and simulating chopping. The model SED is also calculated and compared to the observed fluxes. Simultaneous modeling of the intensity profiles and SED result in nearly orthogonal constraints on the shape of the density profile and the total mass for a given opacity choice (see Shirley et al. 2002). The modeling procedure for PPCs is described in more detail in Evans et al. (2001).

We shall use a family of BE spheres (Ebert 1955, Bonnor 1956) to attempt to fit the L1498 observations since BE spheres were used by Evans et al. (2001) to successfully fit submm continuum observations of other PPCs. BE spheres are solutions to the pressure bounded equations of hydrostatic equilibrium that ignore the effects of magnetic fields and turbulence. The BE density profile is flat in the inner regions and asymptotically approaches r^{-2} in the outer regions. The size of the flat density plateau decreases as the central density of the BE sphere increases (density FWHM = $R(\frac{1}{2}n_c) \sim 1/\sqrt{n_c}$, Chandrasekar & Wares 1949). The temperature structures are characterized by decreasing dust temperature from outside to inside due to extinction of heating radiation from the ISRF. The temperature gradient from outside to inside increases for more centrally condensed BE spheres. Isothermal BE spheres may be parametrized by a single variable, the central density (n_c) for a fixed temperature (10 K). Evans et al. (2001) showed that non-isothermal correction to the shape of the BE profile was negligible for profiles used to describe PPCs. Isothermal BE spheres are calculated with central densities ranging from $\log n_c = 3.5$ to $\log n_c = 7.0$. Since L1498 is embedded within a larger molecular cloud with $A_V \approx 1-3$ mag (Cambr  sy 1999), the power-law portion of the BE profile is not continued below 10^3 cm^{-3} .

Since PPCs lack an internal source, the heating is from the ISRF. The spectrum of the ISRF is derived from *COBE* data (Black 1994) with ultraviolet wavelengths constructed using an empirical description of the radiation field that reproduces the ISRF of Draine (1978; see van Dishoeck 1988). This spectrum is the same as used in the models of Evans et al. (2001). The shape of the ISRF spectrum may be modified by two effects: the intensity of the ISRF (UV to far-infrared) varies at different locations throughout the Galaxy; and the short wavelength intensity of the ISRF (UV to near-infrared) may be modified by dust extinction (see Figure 3). The scaling of the intensity is parametrized by s_{ISRF} while the amount of dust extinction at the core's outer radius is parametrized by A_V . We use

dust opacities appropriate for the general ISM (graphite and silicate based grains, Draine & Lee 1984) to modify the ISRF spectrum. The combination of scaling the ISRF and extinction at the outer core radius is a more realistic description of the incident intensity than has been used in previous models of PPCs.

The reprocessing of the ISRF is strongly affected by the dust opacity within the core. We model the emission using eight different opacities models (see Table 2 and Figure 3). The opacities of Ossenkopf & Henning (1994) are derived from models of grains that have coagulated for 10^5 years and that have acquired varied depths of ice via gas adsorption: OH2 no ice mantles (column 2 Table 5 of Ossenkopf & Henning 1994), OH5 thin ice mantles (column 5, Table 5), and OH8 thick ice mantles (column 8, Table 5). The opacities of Mathis, Mezger, & Panagia (1983) are derived from an empirical fit to dust properties. We also test the opacities of Weingartner & Draine (2001) which describe silicate and graphite grains, including a population of small grains and PAHs, appropriate for the ISM. The opacities of Pollack (1994) describe an alternative grain composition based on silicate grains (olivine and orthopyroxene), iron compounds (troilite and metallic iron), and various organic C compounds. The mass opacity at 850 μm , $\kappa_\nu(850)$, varies by more than one order of magnitude between the opacity models (Table 2). A constant opacity with radius ($R \in [0, R_o]$, R_o is the outer core radius) is assumed throughout the core.

3.2. L1498 Model

A total of 770 radiative transfer models were run that vary n_c , R_o , s_{ISRF} , A_V , and κ_ν . For each model, the reduced χ_r^2 , given by

$$\chi_r^2 = \sum_{i=1}^N \frac{(x_i - x_i^{\text{obs}})^2 / (\sigma_i^{\text{obs}})^2}{N}, \quad (4)$$

was calculated for the 850 and 450 normalized intensity profiles and for the SED. A χ^2 is also calculated for the flux in a $120''$ aperture at 850 μm . The best-fitted models are determined by finding the intersection of the sets of χ_r^2 for each quantity within the typical range $\chi_r^2 \in [0, 1]$. Since the errorbars of the intensity profiles include azimuthal variations as well as intensity uncertainties, and since the errorbars of the SED include an estimate of systematic uncertainty, it is possible for $\chi_r^2 < 1$.

The first grid of models varies n_c and R_o for $s_{\text{ISRF}} = 1$, $A_V = 1$, and OH5 opacities (see top row of Figure 4). The best-fitted model to the azimuthally averaged, normalized intensity profiles is $n_c = 1 \times 10^4 \text{ cm}^{-3}$. If we re-calculate the $\chi_r^2(I_{850})$ using the sector-averaged, normalized intensity profiles, then a wider range of central densities fit, $n_c = 1_{-0.5}^{+2.0} \times 10^4 \text{ cm}^{-3}$ (see dashed profiles in Figure 5d). The best fitted central density does not strongly depend on the size of the outer radius; radii from 30,000 AU to 60,000 AU are well fit. Since emission is clearly detected $100''$ from the center of the SCUBA maps, R_o must be greater than 15,000 AU. Furthermore, the ISO 170 μm image (Ward-Thompson et al. 2002) detects dust emission at radii greater than $200''$ (28,000 AU) from the center; therefore, the best-fitted model R_o are consistent with submillimeter and far-infrared observations.

Since the SCUBA continuum centroid and 1.2 mm continuum peaks are different by $31''$, we have also compared

the dust model intensity profiles to azimuthally averaged intensity profiles centered at the 1.2 mm peak. The best-fitted model are $n_c = 1 - 3 \times 10^4 \text{ cm}^{-3}$ Bonnor-Ebert spheres. This agreement with the best-fitted models toward the SCUBA centroid position is a result of L1498's very flat submillimeter intensity profile that does not vary strongly with different central positions within $\approx 30''$ of the SCUBA continuum centroid (see Figure 1).

The second grid of models varies s_{isrf} , and A_V for the $n_c = 1 \times 10^4$ BE sphere, $R_o = 20,000, 40,000$, and $60,000$ AU, and the different opacity models. The s_{isrf} and A_V are varied on non-linear grids with values between $[0.2, 10]$ and $[0.1, 10]$ respectively. The middle and bottom rows of Figure 4 display $\chi_r^2(\text{SED})$ and $\chi_r^2(S_{850})$ for OH5 dust opacities. Changing s_{isrf} and A_V has a negligible effect on the best fitted normalized intensity profiles; the $n_c = 1 \times 10^4$ BE sphere is the best fit for all opacity models. Previous dust continuum models relied only upon submillimeter fluxes to constrain the heating properties of the ISRF. However, $\chi_r^2(S_{850})$ alone do not strongly constrain s_{isrf} and A_V (bottom row, Figure 5); a wide range of values provide good fits. When we include the complete SED, the s_{isrf} is constrained to be ≤ 2 for the best-fitted models (middle row, Figure 5).

The only dust opacity models that provide satisfactory fits to I_{850} , S_{850} , and the SED are the Ossenkopf & Henning opacities. None of the model $\chi_r^2(\text{SED})$ for WD3, WD4, Pollack1, or Draine-Lee opacities are below 6. These models underestimate the fluxes observed at far-infrared through millimeter wavelengths for the $1 \times 10^4 \text{ cm}^{-3}$ BE sphere. This is not surprising since the mass opacity at $850 \mu\text{m}$ for these models is 3 to 8 times smaller than the mass opacity of OH8 dust. Furthermore, Ossenkopf & Henning opacities for grains with ice mantles (OH5 and OH8) provide better fits to S_{850} and the SED than grains without ice mantles (OH2). The OH2 opacities tend to overestimate S_{850} while underestimating the far-infrared fluxes. It is encouraging that the dust opacities for grains with ice mantles provide the best fits since these models are qualitatively consistent with a physical model of L1498 that accounts for the observed gas depletion of species such as CO, H₂CO, CS, and CCS.

The best-fitted models from all of the model grids are listed in Table 3 and shown in Figure 5. The models fall into two categories: OH5 opacities with $s_{\text{isrf}} \in [1, 2]$ and $A_V \in [4, 8]$; and OH8 and OH5 opacities with $s_{\text{isrf}} \in [0.5, 1]$ and $A_V \in [0.5, 2]$. The fluxes and intensity profiles are well fit at all wavelengths except 1.2 mm for all of the models. All of the best-fitted models have an outer radius of $60,000$ AU (0.29 pc). Since a large outer radius is preferred, it seems unlikely that the high A_V models are physical. An optical extinction map of the Taurus molecular cloud limits the large-scale extinction around L1498 to $A_V \leq 3 \text{ mag}$ (Cambr  s 1999). Indeed, for $A_V = 6$, the column density of material outside R_o would be $N_{H_2} \approx 1 \times 10^{22} \text{ cm}^{-2}$; this value is larger than the column density derived from a $1 \times 10^4 \text{ cm}^{-3}$ BE sphere with $R_o = 60,000$ AU. We prefer the low A_V models as the best, most physical fit.

All of the best-fitted models are characterized by dust temperatures between 10 and 11.1 K (Figure 5a). The low A_V OH5 and OH8 models have temperature gradients of $0.3 < \Delta T_{[0, R_o]} < 0.5 \text{ K}$. These are nearly isothermal tem-

perature profiles compared to previous models of PPCs ($\Delta T_{[0, R_o]} > 1 \text{ K}$, e.g. Evans et al. 2001). The low density of L1498 combined with the inclusion of dust attenuation at the outer radius results in the nearly isothermal temperature profiles.

4. ANALYSIS

4.1. Derived Properties from Continuum Observations

4.1.1. L1498

The bolometric luminosity was calculated by integrating under the spectral energy distribution of L1498 (Table 1) and is $0.12 \pm 0.02 L_\odot$, low for a PPC, but not the lowest reported luminosity (see Table 4). The bolometric temperature, the temperature of a blackbody with the same mean frequency as the observed SED (Chen et al. 1995), is $13.9 \pm 3.1 \text{ K}$. This is one of the lowest bolometric temperatures reported for a PPC (see Table 4).

We calculate the mass from the flux at $850 \mu\text{m}$ in a $120''$ aperture and assuming a constant density, isothermal dust temperature, and optically thin emission using,

$$M_D(T_d) = \frac{S_\nu c^2 D^2}{2h\kappa_\nu \nu^3} \left[\exp\left(\frac{h\nu}{kT_d}\right) - 1 \right] \quad (5)$$

Based on 1D dust radiative transfer models, a dust temperature of $10.5 \pm 0.5 \text{ K}$ is used for L1498. The resulting dust mass, $M_D(10.5 \text{ K}) = 0.67 \pm 0.16 M_\odot$ for an average of OH5 and OH8 opacities ($\bar{\kappa}_\nu(850) = 0.020 \pm 0.002 \text{ cm}^2 \text{ g}^{-1}$). The errors in M_D are propagated from S_ν , T_d , and $\bar{\kappa}_\nu(850)$. L1498's dust mass is consistent with and slightly lower than previously observed pre-protostellar cores ($\langle M_D(10.5) \rangle = 0.9 \pm 0.3 M_\odot$, Table 4).

We also calculate the aperture-averaged column density from the $850 \mu\text{m}$ fluxes using

$$N_{H_2} = \frac{2S_\nu c^2}{h\nu^3 \mu m_H \kappa_\nu \pi \theta_{ap}^2} \left[\exp\left(\frac{h\nu}{kT_d}\right) - 1 \right] \quad (6)$$

The column density at the SCUBA continuum centroid is $(1.25 \pm 0.71) \times 10^{22} \text{ cm}^{-2}$ in a $17''.6$ aperture, where errors are propagated in S_ν , T_d , and $\bar{\kappa}_\nu$. This aperture size matches the BEARS beamsize allowing a direct comparison between dust and N₂H⁺ column density (§4.1.2). The column density corresponds to a visual extinction of $A_V = 13 \text{ mag}$ (Whittet 2003). This extinction is comparable to the peak extinction observed using near-infrared extinction mapping towards the low-density PPC, Coalsack G2 ($A_V = 11.5 \text{ mag}$, Lada et al. 2004). Modeling of the Coalsack G2 extinction profile indicates a peak density of $\approx 10^4 \text{ cm}^{-3}$, corroborating the low density derived for L1498 from our radiative transfer models.

Dust opacities tend to follow a single power-law with frequency at submillimeter wavelengths ($\kappa_\nu \propto \nu^\beta$, $\lambda \in [350, 1300] \mu\text{m}$). The observed dust emissivity index, β , for a core observed at 850 and $450 \mu\text{m}$ is given by,

$$\beta(T_d) = \left[\frac{\log\left(\frac{S_{450}}{S_{850}}\right)}{\log\left(\frac{850}{450}\right)} \right] - \left\{ 3 + \frac{\log\left[\frac{\exp(h\nu_{850}/kT_d)-1}{\exp(h\nu_{450}/kT_d)-1}\right]}{\log\left(\frac{850}{450}\right)} \right\}, \quad (7)$$

where the term in square brackets is the spectral index between 450 and $850 \mu\text{m}$, $\alpha_{450/850}$, and the term in curly braces is the correction for failure of the Rayleigh-Jeans approximation. Assuming a dust temperature of $10.5 \pm 0.5 \text{ K}$, we find $\alpha_{450/850}^{120} = 2.91 \pm 0.61$ and $\beta = 2.44 \pm 0.62$. The

spectral index is higher than all of the PPCs observed by Shirley et al. (2000) except for the two cores associated with L1689A. The β is larger than the theoretical β for dust opacities used in modeling but is consistent, within errors, with all of the dust opacity models except OH2 and WD4 (see Table 2). While OH5 and OH8 opacities give good fits, within errorbars, to the SED, they consistently underestimate the flux at 450 μm while matching the 850 μm flux. Submillimeter measurements of α and β do not discriminate well between opacity models; radiative transfer modeling of the complete SED is a better discriminator.

4.1.2. Comparison with Nearby PPCs

The properties of L1498 may be placed in context by comparing to other PPCs that have been observed with ISO and SCUBA. Table 4 lists observed and derived properties of 10 nearby ($D < 200$ pc) sources. Including the 170 μm ISOPHOT flux gives at least one flux point on the Wien side of the SED, resulting in a more accurate calculation of L_{bol} . Each source SED contains at least 3 flux points (170, 200, and 850 μm). We also analyzed the SCUBA 850 μm images for each source. All of the SCUBA observations are published except for three cores, L183, L1709A, and L63 which were obtained from the CADC SCUBA archive. The reduction procedure for these cores is identical to that described in §2. We have calculated the size, aspect ratio, bolometric luminosity, standard evolutionary indicators (T_{bol} and $\frac{L_{bol}}{L_{smm}}$), and the dust-determined mass from the 850 μm flux. This is a small sample but probably representative of nearby PPCs. The CADC SCUBA archive contains many more observations of PPCs; however, far-infrared observations are needed to calculate L_{bol} .

L1498 is the largest nearby PPC in the sample by 50% and nearly twice as large as the average core size. L1498 also has one of the lowest masses (0.67 M_\odot) of the sample. This is consistent with the interpretation that L1498 is a low density core with a uniquely flat intensity profile. In contrast, the average nearby PPC is a core with 0.14 L_\odot , 0.8 M_\odot , and elongated ($\langle a/b \rangle = 1.6$) with a mean radius of 6000 AU.

PPCs are clearly separated from Class 0 sources on a T_{bol} vs. $\frac{L_{bol}}{L_{smm}}$ diagram (Figure 6). All of the PPCs have low $T_{bol} < 20$ K and $\frac{L_{bol}}{L_{smm}} < 25$ whereas the observed Class 0 sources all have $T_{bol} > 20$ K. T_{bol} and $\frac{L_{bol}}{L_{smm}}$ for PPCs do not correlate. This is not surprising since these evolutionary indicators are strongly influenced by the strength of the ISRF; this is an environmental effect not directly related to the evolutionary state of the core. A better scheme for characterizing the evolutionary state of PPCs would be the comparison of the dynamical maturity determined from radiative transfer models (n_c) and the chemical state of molecules that are abundant at different times. For instance, comparisons of $[\text{CCS}]/[\text{N}_2\text{H}^+]$, comparisons of $[\text{N}_2\text{D}^+]/[\text{N}_2\text{H}^+]$, and the depletion fraction of, f_D , of C^{18}O and H_2CO are promising candidates. The evolutionary state of L1498 is discussed in §4.3.

4.2. Derived Properties from N_2H^+ Observations

The seven hyperfine lines of $\text{N}_2\text{H}^+ J = 1 \rightarrow 0$ were well detected over an extent of $\pm 80''$ in the map (Figure 1f).

The peak T_A^* in the map is coincident with the continuum centroid (Figure 7a). We can estimate the effective density needed to excite an easily observable 1 K N_2H^+ line (see Table 1 of Evans 1999). The critical density of the $J = 1 \rightarrow 0$ is $n_{crit} = 3.8 \times 10^5 \text{ cm}^{-3}$ (collision rates determined from Turner 1995). By analogy with HCO^+ , the resulting effective density (corrected for optically thin hyperfine structure) is $n_{eff} \approx 2 \times 10^4 \text{ cm}^{-3}$, consistent with the derived central density.

The integrated intensity is calculated by integrating over the seven hyperfine components. The $I(T_R^*)$ at the continuum centroid is also the peak in the N_2H^+ map, $I(T_R^*) = 3.92 \pm 0.48 \text{ K km/s}$. The FWHM integrated intensity contour agrees very well with the FWHM continuum contour in size and position angle. The N_2H^+ emission appears to trace the general shape of the continuum emission, but does not peak as sharply along the north-eastern ridge as is seen in the 850 μm and, especially, in the 1200 μm images.

The hyperfine structure was fitted with seven Gaussian functions, constrained by the hyperfine transition velocities (Appendix A), using the profile fitter task in *AIPS++*. The average linewidth was calculated to be $0.22 \pm 0.02 \text{ km/s}$ over the map using the isolated hyperfine component ($JF_1F = 101 \rightarrow 012$). This linewidth is slightly smaller than the linewidth of 0.28 km/s found by Caselli et al. (2002) using the FCRAO. The non-thermal contribution to the linewidth is $\Delta v_{nt} = 0.13 \text{ km/s}$. A plot of the linewidth versus radius (Figure 7b) indicates that the linewidth does not vary significantly out to 15,000 AU ($\approx 110''$). Therefore, the average gas motions in L1498 have low turbulence and are similar throughout the core. This result agrees with the Δv - r relationship towards other PPCs in Taurus observed with BEARS (Tatematsu et al. 2004).

We calculate the virial mass using the Doppler linewidth and assuming an isothermal dust temperature,

$$M_{vir} = \frac{(6R_{FLAT} + 9R_{1/2})}{8G \ln 2} \left[\frac{kT_{iso}}{\mu m_H} + \frac{\Delta v^2}{8 \ln 2} - \frac{kT_{iso}}{m_{amu} m_H} \right]. \quad (8)$$

For a more accurate calculation, we split the radial profile into two sections. The first corresponds to $R \leq R_{FLAT}$ (the radius where $n = 0.9n_c$) which is approximated by a constant density. For a $1 \times 10^4 \text{ cm}^{-3}$ BE sphere, R_{FLAT} is 520 AU. Within the second section, $R_{FLAT} \leq R \leq R_{1/2}$, the density can be approximated by an inverse power law with r^{-2} ($R_{1/2} = 10200 \text{ AU}$, §2.1.2). The term in square brackets converts the observed N_2H^+ linewidth to a 3D velocity dispersion (Shirley et al. 2002). Using the Δv determined above, we find $M_{vir} = 0.84 \pm 0.21 M_\odot$ with errors propagated in $R_{1/2}$, T_{iso} , and Δv . This mass agrees with the mass determined from dust continuum emission (§4.1.1) indicating that L1498 is likely a bound core and that the best-fitted Ossenkopf & Henning dust opacities are appropriate.

The $\text{N}_2\text{H}^+ J = 1 \rightarrow 0$ transition is observed to have moderate optical depths towards low-mass cores (e.g. Tatematsu et al. 2004, Crapsi et al. 2005); therefore, we must calculate the optical depth at each position in the map to derive the column density. For a position-switched observations, theoretically we observe the quantity $T_R = (J_\nu(T_{ex}) - J_\nu(T_{bg}))[1 - \exp(-\tau)]$, where $J_\nu(T) =$

$(h\nu/k)/[\exp(h\nu/kT) - 1]$. This T_R is related to the actual observed quantity, T_A^* , through source-beam coupling and through the efficiency of the antenna (including spillover and atmospheric attenuation, see Kutner & Ulich 1981). Since the hyperfine lines lie close together in frequency ($\Delta\nu < 4.65$ MHz), we assume that the proportionalities for each line are constant (Keto et al. 2004). Therefore, we find the optical depth in the strongest hyperfine component (τ_m , $JF_1F = 123 \rightarrow 112$) by taking ratios of the observed antenna temperatures of the i^{th} hyperfine component to the strongest hyperfine component

$$\frac{(T_A^*)_i}{(T_A^*)_m} = \frac{1 - e^{-R_i\tau_m}}{1 - e^{-\tau_m}}, \quad (9)$$

where R_i is the ratio of relative strengths of the hyperfine lines to the strongest line. R_i is calculated in Appendix A.

The average optical depth in the strongest hyperfine line, $\langle\tau_m\rangle$, was calculated using four of the six observed line ratios and Equation 9. Two of the lines ($JF_1F = 112 \rightarrow 012$ and $110 \rightarrow 011$) consistently gave lower $\langle\tau_m\rangle$ and higher $\langle\tau_m\rangle$ by factors of 0.4 and 2.0 respectively. This may be due to anomalous hyperfine excitation, an effect that has been observed towards other PPCs (Caselli et al. 1995, Turner 2001). An optical depth was determined for 47 positions with suitable signal-to-noise. The optical depth is not affected by line blending since the linewidth is 0.22 km/s (see Appendix A). Since, each hyperfine line has a different optical depth, then correcting the column density using only τ_m would overestimate the column density. We define the average tau by averaging the theoretical hyperfine ratios for the seven observed transitions $\langle\tau\rangle = \frac{1}{7} \sum R_i\tau_m = \frac{27}{49}\tau_m$. The average optical depth in the map is $\langle\tau\rangle_{\text{map}} = 0.83 \pm 0.54$, indicating that the N_2H^+ $J = 1 \rightarrow 0$ transition is moderately optically thick over most of the map. As an example, the SCUBA continuum centroid position has an optical depth of $\langle\tau\rangle = 1.11 \pm 0.61$, resulting in a correction for optical depth to the column density of $\langle\tau\rangle/(1 - e^{-\langle\tau\rangle}) = 1.66^{+0.43}_{-0.38}$.

The total column density for N_2H^+ is (see Goldsmith & Langer 1999)⁷

$$N_{\text{N}_2\text{H}^+} = \frac{3kQ(T_{ex})\exp(E_u/kT_{ex})}{8\pi^3\nu\mu^2J_u} \frac{\langle\tau\rangle}{1 - e^{-\langle\tau\rangle}} \int \frac{T_A^*}{\eta_{\text{mb}}} dv, \quad (10)$$

where $Q(T_{ex})$ is the rotational partition function and $\mu = 3.4$ D (Green et al. 1974) is the dipole moment. We assume an excitation temperature of 10 ± 5 K. Errors in $N_{\text{N}_2\text{H}^+}$ are propagated for T_{ex} , $\langle\tau\rangle$, and $I(T_R^*)$. The peak column density is $(8.3 \pm 3.4) \times 10^{12} \text{ cm}^{-2}$ with an average column density of $(3.5 \pm 2.1) \times 10^{12} \text{ cm}^{-2}$. The peak column density agrees remarkably well with the calculation of Caselli et al. (2002a) for lower resolution FCRAO 15 m N_2H^+ observations towards L1498 $((8 \pm 4) \times 10^{12} \text{ cm}^{-2})$ and the intermediate resolution IRAM 30 m observations of Crapsi et al. (2005; $(7.1 \pm 0.7) \times 10^{12} \text{ cm}^{-2}$).

We calculate the abundance, $X_{\text{N}_2\text{H}^+}(R) = N_{\text{N}_2\text{H}^+}(R)/N_{\text{H}_2}(R)$, by comparing the N_2H^+ column density to the beam averaged column density determined from the 850 μm dust continuum map (Equation 6). The average column density in the map is

$\langle X_{\text{N}_2\text{H}^+} \rangle_{\text{map}} = (4.0 \pm 3.7) \times 10^{-10}$ relative to H_2 . This column density agrees very well with the early-time abundances of the coupled dynamical-chemical models of Lee et al. (2004) for quasi-statically evolving PPCs (§4.3). The abundance show no significant variations with radius out to 15,000 AU, although the errors on the abundance are sizable (Figure 7d). Radiative transfer models of the N_2H^+ emission should assume a constant abundance of $\approx 4 \times 10^{-10}$.

The N_2H^+ $J = 3 \rightarrow 2$ transition was not detected towards the continuum centroid position with a $1\sigma(T_R^*)$ baseline rms of 45 mK (Figure 7c); however, Crapsi et al. (2005) report a detection with the IRAM 30 m toward the 1.2 mm continuum peak position ($T_A^* = 380 \pm 53$ mK; see inset in Figure 7c). This is puzzling since the $J = 1 \rightarrow 0$ BEARS map shows no enhancement toward that position. It is possible that the 1.2 mm continuum peak represents the true density peak of L1498. A high-resolution, over-sampled map of the N_2H^+ $J = 3 \rightarrow 2$ emission is needed to resolve this discrepancy. The exact location of the density peak will be important for molecular line radiative transfer modeling, but does not affect the conclusions from dust continuum modeling (§3.2).

The L1498 N_2H^+ observations will be modeled, along with other PPCs, in a future paper.

4.3. Derived Properties from C_3S Observations

The C_3S $J = 4 \rightarrow 3$ line was strongly detected toward L1498 (Figure 8) and the emission follows the same double-peaked pattern as previous observations of CS and CCS (Figure 1 of Willacy, Langer, & Velusamy 1998). The line intensity is strongest in the southeastern peak ($T_R^* = 1.64 \pm 0.35$ K) at J2000.0 $\alpha = 4^{\text{h}} 10^{\text{m}} 56.9^{\text{s}}$, $\delta = +25^\circ 9' 22''.5$. Since the C_3S emission has an intensity saddle at the SCUBA dust continuum centroid, it is another excellent example of strong chemical differentiation in L1498. The southeastern C_3S peak does not exactly correspond to the Willacy, Langer, & Velusamy CS or CCS peak, but instead lies between them and closer to the CS peak. Combination of the GBT observations with higher resolution observations (e.g., VLA) would improve the peak position and may confirm slight chemical differentiation between all of the observed sulfur-carbon chain molecules.

The C_3S $J = 4 \rightarrow 3$ linewidth was measured using the Gaussian fitting routine is *AIPS++* toward 42 positions in the map with detections greater than 3σ . The average linewidth is $\Delta\nu = 0.21 \pm 0.03$ km/s, consistent with the N_2H^+ linewidth. No significant variation of $\Delta\nu$ is also seen for C_3S with radius (Figure 8b).

The column density of C_3S was estimated using the same method as for N_2H^+ (Equation 10). We estimate the optical depth of the C_3S $J = 4 \rightarrow 3$ with 10 minute observations at the southeastern peak position of three isotopologues. The detection of C_3^{34}S $J = 4 \rightarrow 3$ (Figure 8c; $T_A'(\text{C}_3\text{S})/T_A'(\text{C}_3^{34}\text{S}) = 19.7 \pm 3.1$) and lack of a significant detection ($> 3\sigma$) of ^{13}CCS or C^{13}CCS $J = 4 \rightarrow 3$, indicates, for the standard ISM isotope ratios of $[^{32}\text{S}]/[^{34}\text{S}] = 22$ and $[^{12}\text{C}]/[^{13}\text{C}] = 77$ (Wilson & Rood 1994), that the C_3S emission is consistent with being optically thin. The

⁷ This derivation of the correction for an optically thick column density should not be confused with estimates based on the total optical depth, $\tau_{\text{tot}} = \frac{27}{7}\tau_m$ (e.g. Caselli et al. 2002b).

peak column density is $N_{\text{C}_3\text{S}} = (5.0 \pm 1.8) \times 10^{12} \text{ cm}^{-2}$ and is less than a factor of 2 less than the peak CCS column density determined by Wolkovitch et al. (1997) ($8.7 \times 10^{12} \text{ cm}^{-2}$).

The abundance of C_3S was calculated by comparing the C_3S column density to the column density derived from the $850 \mu\text{m}$ map in $33''$ apertures. Since the C_3S emission is very asymmetrical, we plot the abundance versus radius in the major-axis sector (§2.1.2) in Figure 8d. Negative radii refer to positions SE of the dust continuum centroid. The depletion of C_3S is clearly visible with enhanced abundances by factors of 4.8 and 2.3 at the two C_3S intensity peaks. The abundance is largest in the SE peak ($X_{\text{C}_3\text{S}} = (4.5 \pm 2.4) \times 10^{-10}$). The abundance peaks are symmetrically located at a radius of 9500 AU from the dust continuum centroid position. This radius set a limit for the depletion radius of C_3S , corresponding to a density of $0.8 - 1.5 \times 10^4 \text{ cm}^{-3}$ for the best-fitted BE spheres. Since the abundance pattern of C_3S is similar to smaller sulfur-carbon chain molecules (e.g., CS and C_2S), the southeastern C_3S peak of L1498 would be an excellent site to search for larger sulfur-carbon chain molecules such as C_4S and C_5S (Gordon et al. 2001).

4.4. Interpretation of Density Structure

Radiative transfer modeling of submillimeter images combined with far-infrared and millimeter photometry indicate that L1498 is a low density, nearly isothermal PPC, with a low strength of the ISRF and dust opacities appropriate for coagulated, icy grains. The central density of $1 - 3 \times 10^4 \text{ cm}^{-3}$ is the among lowest central densities reported for PPCs, similar to Coalsack G2 (Lada et al. 2004). This density range agrees with the densities determined by Langer & Willacy (2001) from analysis of ISO observations of L1498 ($1.2 - 5.5 \times 10^4 \text{ cm}^{-3}$ with lower densities more appropriate for larger core radii). However, our modeling results differ substantially from the analytical model of Tafalla et al. (2004) which fits the radial profile of L1498 at 1.2 mm with a function of the form $n(r) = n_c/[1 + (r/R_{1/2})^p]$ and assumes an isothermal dust temperature profile of $T_d(r) = 10 \text{ K}$. Tafalla et al. find a central density of $9.5 \times 10^4 \text{ cm}^{-3}$, three times larger than the maximal BE central density in our models. There are a few discrepancies that may account for this difference. Tafalla assume a dust opacity of $5 \times 10^{-3} \text{ cm}^2 \text{ g}^{-1}$ at 1.2 mm that is a factor of 2 smaller than OH5 opacities ($1.02 \times 10^{-3} \text{ cm}^2 \text{ g}^{-1}$). Since the column density is inversely proportional to the opacity, the Tafalla et al. opacity would result in a factor of 2 larger central density. This does not account for the full difference between the results. The Tafalla et al. centroid position is located at the peak of the non-axisymmetry which is much more pronounced at 1.2 mm than at submillimeter wavelengths. Tafalla et al. calculate a column density of $3 - 4 \times 10^{22} \text{ cm}^{-2}$, a factor of 3 higher than our column density determined at $850 \mu\text{m}$. For all of the best-fitted radiative transfer models, the 1.2 mm flux is always underestimated while the other six fluxes (170, 200, 450, 850, 1100, and $1300 \mu\text{m}$) are fit within the errorbars. The 1.2 mm flux point appears to be anomalously high. It is possible that calibration uncertainties may account for the remaining difference.

The low density implies that L1498 is dynamically young. Indeed, L1498 may be in a stable hydrostatic state. One measure of stability of BE spheres is the density gradient between inside and outside of the core. If the density contrast exceeds 14.3, then the BE sphere is in an unstable equilibrium (see Foster & Chevalier 1993). A lower density limit of 10^3 cm^{-3} was assumed for the core in the radiative transfer models. This lower limit was chosen to be larger than the average density in a molecular cloud (10^2 cm^{-3}) since L1498 is situated within an extended condensation of 1 to 3 A_V in the Taurus-Auriga molecular cloud (see Cambr  s 1999). The average solution ($1 \times 10^4 \text{ cm}^{-3}$) is stable, but this results depends sensitively on the density at the outer radius. For the maximal central density ($3 \times 10^4 \text{ cm}^{-3}$), the density contrast is 30 and the core is unstable. Unfortunately, we cannot strongly constrain the density contrast since the submillimeter observations are insensitive to structure outside the chop distance ($120''$ or 16,800 AU).

A more quantitative way to test the stability is to directly compare the Jeans mass with the mass of the BE sphere. The Jeans Mass for $T = 10.5 \text{ K}$ and $n = 10^4 \text{ cm}^{-3}$ is $M_J \approx 18T^{3/2}n^{-1/2} = 5.7 M_\odot$ (Spitzer 1978), while the $1 \times 10^4 \text{ cm}^{-3}$ BE sphere has a mass of $M_{BE} \approx 1.15(T/10\text{K})(P_0/10^5 \text{ K cm}^{-3})^{-1/2} = 3.6 M_\odot$ (Bonnor 1956). The BE mass is within a factor of 2 of the Jeans mass, but $M_{BE} < M_J$. If we use the $3 \times 10^4 \text{ cm}^{-3}$ BE sphere, then the mass is comparable to the Jeans mass $M_J = 3.3 M_\odot$. This mass comparison is consistent with L1498 being a core that is marginally stable to gravitational collapse.

While L1498 may be dynamically unevolved, it appears to be chemically evolved. Species such as H_2CO , CS, CCS, and C_3S (e.g., Willacy et al. 1998, Tafalla et al. 2004, Young et al. 2004, §4.3) are depleted towards the center of the core. We can estimate the depletion timescale from the rate equation given in Rawlings et al. (1992). For a depletion fraction, f_D , the adsorption timescale of a neutral molecular species, i , is given by,

$$t_{\text{adsorp}}(i) = \frac{1.38 \times 10^9 \ln(1/f_D) m_i^{1/2}}{n S_i T^{1/2}} \text{ yrs.}, \quad (11)$$

where m_i is the molecular mass in a.m.u. and S_i is the sticking coefficient (also see Charnley, Rodgers, & Ehrenfreund 2001). For example, H_2CO has been observed to be severely depleted towards L1498 over a large spatial extent (Wang 1994; Young et al. 2004). The adsorption timescale is $t_{\text{adsorp}}(\text{H}_2\text{CO}) \approx 5.5 \times 10^5$ years for $f_D = 1/10$, $S_i = 1$, and $T = 10.5 \text{ K}$ in the absence of other formation or destruction mechanism. In reality, many chemical effects may affect this timescale. Two of the first molecules to be depleted are CCS and C_3S . Comparisons with detailed coupled dynamical-chemical models indicate that the CCS becomes depleted on timescales of a few 10^5 years (e.g., Li et al. 2002, Aikawa et al. 2003, Lee et al. 2004).

A chemical age of a few 10^5 years is consistent with the observed abundance of N_2H^+ (Aikawa et al. 2003, Lee et al. 2004). N_2H^+ is considered a ‘‘late time’’ species since it is primarily destroyed in the gas phase by CO and its abundance increases after CO is significantly adsorbed (although dissociative recombination may also be important at low densities, see Geppert et al. 2004). Detailed chemical models indicate that this abundance increase occurs

after $\approx 10^5$ years (e.g. Aikawa et al. 2003). Clearly, L1498 must have been in a stable or very slowly evolving configuration for at least 10^5 years to display the extreme molecular depletion and modest N_2H^+ abundance that is observed.

The dust opacities that best-fitted the L1498 SED were Ossenkopf & Henning opacities (1994) for grains that had coagulated for 10^5 years and accreted ice mantles (OH5 & OH8). These opacities have also successfully fit the SEDs of low-mass embedded protostars (e.g., Shirley et al. 2002) and high-mass embedded protostars (e.g., Mueller et al. 2002). The OH opacities are qualitatively consistent with the observed molecular depletion and the chemical timescale for L1498; however, the coagulation simulation of OH5 and OH8 assumes a density of $n_{\text{H}_2} = 10^6 \text{ cm}^{-3}$ sustained for 10^5 years (see Ossenkopf 1993). This density is substantially higher than the density derived from dust continuum models; therefore, the OH5 and OH8 opacities may not be based on an accurate representation of fluffy aggregation of grains in low density PPCs.

How do you create a dynamically young yet chemically evolved core? If L1498 is in an unstable equilibrium, it cannot have been in that state for a long period of time since the free-fall time for a $1 - 3 \times 10^4 \text{ cm}^{-3}$ BE sphere, $t_{\text{ff}} = \sqrt{3\pi/8G\mu m_{\text{H}} n}$ (Spitzer 1978), is approximately $3 - 1.7 \times 10^5$ years. Clearly, L1498 has not yet collapsed and displays chemical differentiation that requires a similar timescale. L1498 must have been static or slowly collapsing for more than 10^5 years. While magnetic fields may also play a significant role in cloud support and evolution for dynamically nascent PPCs (e.g. Mouschovias & Spitzer 1976, Li et al. 2002), in the case of L1498, they are not necessary for support of the cloud (since $M_{\text{BE}} < \text{or } \approx M_{\text{J}}$). Nevertheless, we can estimate the strength of the B-field required for equipartition of magnetic, gravitational, and kinetic energy. The strength of this B-field is given by $B \approx 0.51 n^{1/2} \Delta v_{\text{nt}} (\text{km/s}) = 8.7 \mu\text{G}$ (Lada et al. 2004). This is a small magnetic field compared with Zeeman measurements of the CCS $J_N = 3_2 \rightarrow 2_1$ transition which provide a rough estimate of the line-of-sight field strength of $48 \pm 31 \mu\text{G}$ (Levin et al. 2001). If L1498 becomes massive enough to be unstable to gravitational collapse, then the magnetic field appears to be strong enough to support L1498, in which case, the timescale for collapse is controlled by the ambi-polar diffusion timescale until the core becomes magnetically super-critical.

Recent molecular line studies of PPCs in the Taurus-Auriga molecular cloud have identified cores (e.g. L1521B and L1521E) that appear to be dynamically young and chemically young (Hirota et al. 2002; Tafalla & Santiago 2004; Hirota, Maezawa, & Yamamoto 2004). The signature of chemical youth is strongly peaked sulfur-bearing carbon chain molecules (e.g., CCS and C_3S), weak NH_3 and N_2H^+ emission, and low molecular depletion of C^{18}O . Confirmation of the chemical and dynamical youth of these cores requires a detailed comparison between submillimeter dust continuum emission and high-resolution observations of CCS or C_3S . These objects, along with L1498, L1512 ($n_c = 10^5 \text{ cm}^{-3}$), and L1544 ($n_c = 10^6 \text{ cm}^{-3}$) may represent an evolutionary sequence in Taurus-Auriga where chemical maturity is reached first and then dynamical evolution occurs (see Figure 9).

An important caveat is that our 1D modeling has ignored the observed non-axisymmetry in L1498. The dust continuum emission peaks along the north-east ridge and not at the FWHM centroid. This effect is most pronounced in the 1.2mm but is also detected at $850 \mu\text{m}$. Other PPCs (e.g., L1544 and L63) also display clear non-axisymmetries. The spherical BE model is limited and unable to describe this structure. A full 3D radiative transfer modeling is needed to probe the structure of the non-axisymmetry (e.g. Doty et al. 2004). Also, since the $90 \mu\text{m}$ ISO image (Ward-Thompson et al. 2002) shows a clear gradient across the image, there is evidence that the ISRF asymmetrically heats L1498 (also see Langer & Willacy 2001). 3D models could explore triaxial, BE-like model with a spatially varying ISRF compared to fully non-axisymmetric density distributions (see Gonçalves, Galli, & Walmsley 2004). Encouragingly, a comparison between 3D models and 1D models of L1544 indicate that the 1D models are an acceptable fit to the average physical structure (Doty et al. 2004).

5. CONCLUSION

We have presented deep SCUBA observations, BEARS and CSO N_2H^+ observations, and GBT C_3S observations of the Pre-protostellar core, Lynds 1498. Radiative transfer modeling of the submillimeter intensity profiles and the complete SED were performed. Our main conclusions are as follows.

L1498 is characterized by a low density Bonnor-Ebert sphere with central density of $1 - 3 \times 10^4 \text{ cm}^{-3}$ and outer radius greater than 40,000 AU. The SED is best-fitted with Ossenkopf & Henning opacities for coagulated grains with thick and thin ice mantles (OH8 and OH5 opacities). A more realistic treatment of the ISRF was used that includes variations in the strength of the incident specific intensity and extinction due to dust grains at the outer radius of the core. L1498 is a potentially stable ($M_{\text{BE}} < M_{\text{J}}$), magnetically sub-critical core that appears to be dynamically young. These results do not change if the 1.2 mm continuum peak is used for the radial intensity profiles instead of the SCUBA continuum centroid.

Observations of the depletion of species such as C_3S and H_2CO indicate L1498 is chemically evolved ($t > 10^5$ years). The modest N_2H^+ abundance is also consistent with a chemically evolved source. The best-fitted Ossenkopf & Henning opacities are consistent with this timescale, although the Ossenkopf coagulation models assume a higher density than is observed toward L1498. The N_2H^+ and C_3S linewidth do not vary significantly with radius out to 15,000 AU. The N_2H^+ abundance also does not vary significantly with radius, while the C_3S abundance indicates significant depletion toward the center of L1498.

Comparisons of L1498 with nearby PPCs that have also been observed at far-infrared and submillimeter wavelengths indicate that L1498 is larger than average, less luminous than average, and less massive than average. The standard evolutionary indicators used for low-mass protostars, T_{bol} and $\frac{L_{\text{bol}}}{L_{\text{smm}}}$, do not correlate for PPCs. All of the PPCs in this sample are characterized by $T_{\text{bol}} < 20 \text{ K}$ and $\frac{L_{\text{bol}}}{L_{\text{smm}}} < 25$.

The temperature and density structure derived from 1D models may now be used in more realistic models of molec-

ular line emission. Future studies of PPCs require high resolution far-infrared observations coupled with 3D radiative transfer modeling of multiple wavelengths. Instruments

such as HAWC on SOFIA and the launch of HERSCHEL will provide the needed high resolution far-infrared observations.

APPENDIX

HYPERFINE LEVELS OF N_2H^+ $j = 1 \rightarrow 0$

Since every nucleus in the N_2H^+ molecules has non-zero nuclear spin, N_2H^+ has a very rich hyperfine spectrum that can be exploited to probe the physical conditions in star-forming regions. In this appendix, we summarize the hyperfine splitting of the ground state rotational transition of N_2H^+ .

The hyperfine splitting (in order of importance) is due to: (1) an electric quadrupole interaction due to the outer nitrogen; (2) an electric quadrupole interaction due to the inner nitrogen; (3) a magnetic dipole interaction due to the outer nitrogen; (4) a magnetic dipole interaction due to the inner nitrogen; (5) a magnetic dipole interaction due to the hydrogen nucleus; and (6) spin-spin interactions between the nuclei. The final two effects are ignored in calculations of hyperfine splitting for astronomical sources since the observed linewidth is > 0.1 km/s (> 31 kHz) and the hyperfine coupling constants are small (see Caselli, Myers, & Thaddeus 1995).

There are 15 electric dipole allowed transitions for N_2H^+ $J = 1 \rightarrow 0$ in the $|JF_1F\rangle$ basis ($\Delta J = -1$, $\Delta F_1 = 0, \pm 1$, $\Delta F = 0, \pm 1$, $0 \not\rightarrow 0$). The 15 transitions are listed in Table 5; however, since in practice the $J = 0$ level is not split, degenerate transitions are collected together into the 7 observed transitions. We adopt the standard notation from Caselli, Myers, & Thaddeus for the transition labels (1995).

It is convenient to calculate the ratio of relative strengths, R_i , of the hyperfine levels for calculations of optical depth and column density (§4.2). The relative strengths, s_i , are determined using irreducible tensor methods (Gordy & Cook 1984, Chapter 15) and are defined such that the sum of the relative strength of the electric dipole allowed transitions are equal to one (see Rudolph 1968). The ratio of relative strengths for the N_2H^+ $J = 1 \rightarrow 0$ transitions in the $|JF_1F\rangle$ basis are given by

$$R_i(1F_1'F' \rightarrow 0F_1F) = \sum_{\substack{\text{allowed} \\ F' \rightarrow F}} \frac{3}{7} \left\{ \begin{matrix} 1 & F_1' & 1 \\ 1 & 0 & F_1 \end{matrix} \right\}^2 \left\{ \begin{matrix} 1 & F' & F_1' \\ 1 & F_1 & F \end{matrix} \right\}^2 \prod_{F_i=F_1', F_1, F', F} (2F_i + 1), \quad (\text{A1})$$

where the 6-j symbols needed in Equation A1 may be found in Table 5 of Edmonds (1974). The ratios must be summed over the degenerate transitions from the same $J = 1 F_1' F'$ level (Table 5).

It is necessary to calculate the dependence of R_i on the linewidth for closely spaced hyperfine lines (see Turner 2001). We have performed this calculation for the N_2H^+ $J = 1 \rightarrow 0$ transitions assuming each hyperfine component is Gaussian,

$$R_i(\Delta v) = \frac{\sum_{j=1}^7 s_j \exp \left[-4 \ln 2 \frac{(v_j - v_i)^2}{\Delta v^2} \right]}{\sum_{j=1}^7 s_j \exp \left(-4 \ln 2 \frac{v_j^2}{\Delta v^2} \right)}. \quad (\text{A2})$$

The results are shown in Figure 10. For sources with $\Delta v \leq 0.3$ km/s, the theoretical hyperfine ratios are sufficient. This is the case for L1498. However, for N_2H^+ observations of sources with broader linewidths, the linewidth-corrected R_i should be used.

ACKNOWLEDGMENTS

We wish to thank the staffs of the NRO, JCMT, CSO, and GBT for their excellent assistance. We are very grateful to Mario Tafalla and Derek Ward-Thompson for providing us 1.2 mm and 170 μm images of L1498, to Luca Dore for providing us his calculation of the N_2H^+ $J = 3 \rightarrow 2$ hyperfine frequencies, and to Antonio Crapsi for providing IRAM 30 m spectra of the N_2H^+ $J = 3 \rightarrow 2$ transition. We especially thank Ron Maddalena for assistance with GBT calibration. George Moellenbrock, Kumar Golap, and Joe McMullan provided excellent assistance with Glish scripting in AIPS++. Finally, we thank the referee for a very detailed and helpful review. NJE acknowledges support from Grant AST-030725 from the National Science Foundation and NASA Grants NAG5-10488 and NNG04GG24G.

REFERENCES

- Adams, F. C. 1991, *ApJ*, 382, 544
- Aikawa, Y., Ohashi, N., & Herbst, E. 2003, *ApJ*, 593, 906
- Alves, J., Lada, C. J., & Lada, E. A. 2001, *Nature*, 409, 159
- Archibald, E.N., et al. 2002, *MNRAS*, 336, 1
- Bianci, S., Gonçalves, J., Albrecht, M., Caselli, P., Chini, R., Galli, D., & Walmsley, M. 2003, *A&A*, 399, L43
- Black, J. H. 1994, *ASP Conf. Ser.* 58, *The First Symposium on the Infrared Cirrus and Diffuse Interstellar Clouds*, ed. R.M. Cutri & W.B. Latter (San Fransico:ASP), 355
- Bonnor, W. B. 1956, *MNRAS*, 116 351
- Buisson, G., Desbats, L., Duvert, G., Forveille, T., Gras, R., Guilloteau, S., Lucas, R., & Valiron, P. 2002, *Continuum and Line Analysis Single-dish System Manual*
- Cambr  sy, L. 1999, *A&A*, 345, 965
- Caselli, P., Myers, P. C., & Thaddeus, P. 1995, *ApJ*, 455, L77
- Caselli, P., Benson, P.J., Myers, P.C., & Tafalla, M. 2002a, *ApJ*, 572, 238
- Caselli, P., Walmsley, C. M., Zucconi, A., Tafalla, M., Dore, L., & Myers, P. C. 2002b, *ApJ*, 565, 344
- Chen, H. Myers, P. C., Ladd, E. F., & Wood, D. O. S. 1995, *ApJ*, 445, 377
- Chandrasekar, S., & Wares, G. W. 1949, *ApJ*, 109, 551

- Charnley, S. B., Rodgers, S. D., & Ehrenfreund, P. 2001, *A&A*, 378, 1024
- Crapsi, A., Caselli, P., Walmsley, C. M., Myers, P. C., Tafalla, M., Lee, C. W., & Bourke, T. L. 2005, *ApJ*, 619, 379
- Doty, S. D., Everett, S. E., Shirley, Y. L., Evans, N. J., II, Palotti, M. L. 2004, *MNRAS* submitted
- Draine, B. T. 1978, *ApJS*, 36, 595
- Draine, B. T., & Lee H. M. 1984, *ApJ*, 285, 89
- Ebert, R. 1955, *ZAp*, 37, 217
- Edmonds, A.R. 1974, *Angular Momentum in Quantum Mechanics*, 3rd ed., (Princeton University Press: Princeton, New Jersey)
- Egan, M. P., Leung, C. M., & Spagna, G. F., 1988, *Comput. Physics Comm.*, 48, 271
- Elias, J. 1978, *ApJ*, 224, 453
- Evans, N. J., II 1999, *ARA&A*, 37, 311
- Evans, N.J., II, Rawlings, J.M.C., Shirley, Y.L., & Mundy, L.G. 2001, 557, 193
- Flower, D. R., Pineau des Forêts, G., & Walmsley, C. M. 2005, *A&A*, in press (astro-ph/0503501)
- Foster, P. N., Chevalier, R. A. 1993, *ApJ*, 416, 303
- Hirota, T., Ito, T., & Yamamoto, S. 2002, *ApJ*, 565, 359
- Hirota, T., Maezawa, H., & Yamamoto, S. 2004, *ApJ*, in press (astro-ph/0409105)
- Geppert et al. 2004, *ApJ*, 609, 459
- Goldsmith, P. F., & Langer, W. D. 1999, *ApJ*, 517, 209
- Gonçalves, J., Galli, D., & Walmsley, M. 2004, *A&A*, 415, 617
- Gordon, V. D., McCarthy, M. C., Apponi, A. J., & Thaddeus, P. 2001, *ApJS*, 131, 311
- Gordy, W., & Cook, R.L. 1984, *Microwave Molecular Spectroscopy* 3rd ed., in *Techniques of Chemistry* vol.17, (John Wiley & Sons:New York)
- Green, S., Montgomery Jr., J. A., & Thaddeus, P. 1974, *ApJ*, 193, L89
- Greisen, E. & Harten 1981, *A&AS*, 44, 371
- Ivezić, Ž., Nenkova, M. & Elitzur M. 1999, User Manual for *DUSTY*, University of Kentucky Internal Report
- Jenness, T., & Lightfoot, J.F. 1997, *SURF - SCUBA User Reduction Facility* ver. 1.1 User's Manual, Starlink User Note 216 (Hilo: Joint Astronomy Centre)
- Jijina, J., Myers, P. C., & Adams 1999, *ApJS*, 125, 161
- Jørgensen, J. K., Schöier, F. L., & van Dishoeck, E. F. 2002, *A&A*, 389, 908
- Keto, E. Rybicki, G. B., Bergin, E. A., & Plume, R. 2004, *ApJ*, in press (astro-ph/0407433)
- Kooi, J. W., Chan, M., Phillips, T. G., Bumble, B., & Leduc, H. G. 1992, *IEEE trans. Microwaves Theory and Techniques*, 40, 812
- Kuiper, T.B.H., Langer, W.D., & Velusamy, T. 1996, *ApJ*, 468, 761
- Kutner, M. L., & Ulich, B. L. 1981, *ApJ*, 250, 341
- Lada, C. J., Huard, T. L., Crews, L. J., & Alves, J. F. 2004, *ApJ*, 610, 303
- Lai, S.-P., Velusamy, T., Langer, W. D., & Kupier, T. B. 2003, *ApJ*, 126, 311
- Langer, W. D., & Willacy K. 2001, *ApJ*, 557, 714
- Langston, G., Braatz, J., Ghigo, F., Maddalena, R., Minter, T., & O'Neal, K. 2004, GBT Commissioning Memo #24
- Lee, J.-E., Bergin, E. A., Evans, N. J., II 2004, *ApJ*, in press (astro-ph/0408091)
- Lemme, C., Walmsley, C. M., Wilson, T. L., & Muders, D. 1995, *A&A*, 302, 509
- Levin, S. M., Langer, W. D., Velusamy, T., Kuiper, T. B. H., & Crutcher, R. M. 2001, *ApJ*, 555, 850
- Li, Z.-Y., Shematovich, V. I., Wiebe, D. S., & Shustov, B. M. 2002, *ApJ*, 569, 792
- Mathis, J. S., Mezger, P. G., & Panagia, N. 1983, *A&A*, 128, 212
- Mouschovias, T. C., & Spitzer, L., Jr. 1976, *ApJ*, 210, 326
- Myers, P.C., & Benson, P.J. 1983, *ApJ*, 266, 309
- Mueller, K. E., Shirley, Y. L., Evans, N. J., II, & Jacobson, H. R. 2002, *ApJS*, 143, 469
- Müller, H. S. P., Thorwirth, S., Roth, D. A., & Winnewisser, G. 2001, *A&A*, 370, L49
- Ossenkopf, V. 1993, *A&A*, 280, 617
- Ossenkopf, V., & Henning, Th. 1994, *A & A*, 291, 943
- Penzias, A. A., & Burrus, C. A. 1973, *ARA&A*, 11, 51
- Pollack, J. B., Hollenbach, D., Beckwith, S., Simonelli, D. P., Roush, T., & Fong, W. 1994, *ApJ*, 421, 615
- Rawlings, J.M.C., Hartquist, T.W., Menten, K.M., & Williams, D.A. 1992, *MNRAS*, 255, 471
- Rohlfs, K., & Wilson T. L. 2000, *Tools of Radio Astronomy* (Springer Verlag: Berlin) 194 - 198
- Rudolph, H. D. 1968, *Z. Naturforsch.*, 23a, 540
- Taylor, S.D., Morata, O., & Williams, D.A. 1996, *A&A*, 313, 269
- Tafalla, M., Myers, P. C., Caselli, P., Walmsley, C. M., & Comito, C. 2002, *ApJ*, 569, 819
- Tafalla, M., Myers, P. C., Caselli, P., & Walmsley, C. M. 2004, *A&A*, 416, 191
- Tafalla, M., & Santiago, J. 2004, *A&A*, 414, L53
- Turner, B. E. 1995, *ApJ*, 449, 635
- Turner, B. E. 2001, *ApJS*, 136, 579
- Shirley, Y. L., Evans, N.J., Rawling, J.M.C., & Gregersen, E.M. 2000, *ApJS*, 131, 249
- Shirley, Y. L., Evans, N.J., & Rawling, J.M.C. 2002b, *ApJ*, 575, 337
- Shirley Y. L., Mueller, K. E., Young, C. H., Evans, N. J., II 2003, in *Galactic Star Formation Across the Stellar Mass Spectrum*, ed. J. M. De Buizer, ASP conference series 287, 298
- Spitzer, L., Jr. 1978, *Physical Processes in the Interstellar Medium*, (John Wiley & Sons: New York) 287
- Stamatellos, D., & Whitworth, A. P. 2004, (*astro-ph/0406549*)
- Sunada, K., Yamaguchi, N., Kuno, S., Okumura, S., Nakai, N., & Ukitu, N. 2000, in *Imaging at Radio through Submillimeter Wavelengths*, ASP Conference Series, 217, 19
- Tatematsu, K. Umemoto, T., Kandori, R., & Sekimoto, Y. 2004, *ApJ*, 606, 333
- van Dishoeck, E. F. 1988, *Rate Coefficients in Astrochemistry*, ed. T.L. Millar & D.A. Williams (Astrophys. & Space Sci. Library;Dordrecht:Kluwer),49
- Wang, Y. 1994, Ph.D. Thesis, The University of Texas at Austin
- Ward-Thompson, D., Scott, P. F., Hills, R. E., & André, P. 1994, *MNRAS*, 26 8, 276
- Ward-Thompson, D., Motte, F., & André, P. 1999, *MNRAS*, 305, 143
- Weingartner, J. C., & Draine, B. T. 2001, *ApJ*, 548, 296
- Whittet, D. C. B. 2003, *Dust in the Galactic Environment*, Second ed. (IOP Publishing: Philadelphia), 11
- Willacy, K., Langer, W.D., & Velusamy, T. 1998, *ApJL*, 507, 171
- Wilson, T. L., & Rood R. 1994, *ARA&A*, 32, 191
- Wolkovitch, D., Langer, W. D., Goldsmith, P. F., & Heyer, M. 1997, *ApJ*, 477, 241
- Langer, W. D., & Willacy, K. 2001, *ApJ*, 557, 714
- Young, C. H., Shirley, Y. L., Evans, N. J., II, & Rawlings, J. M. C. 2003, *ApJS*, 145, 111
- Young, K. E., Lee, J.-E., Evans II, N. J., Goldsmith, P. F., & Doty, S. 2004, *ApJ*, in press
- Zhou, S., Evans II, N. J., Wang, Y., Peng, R., & Lo, K. Y. 1994, *ApJ*, 433, 131
- Zucconi, A., Walmsley, C. M., & Galli, D. 2001, *A&A*, 376, 650

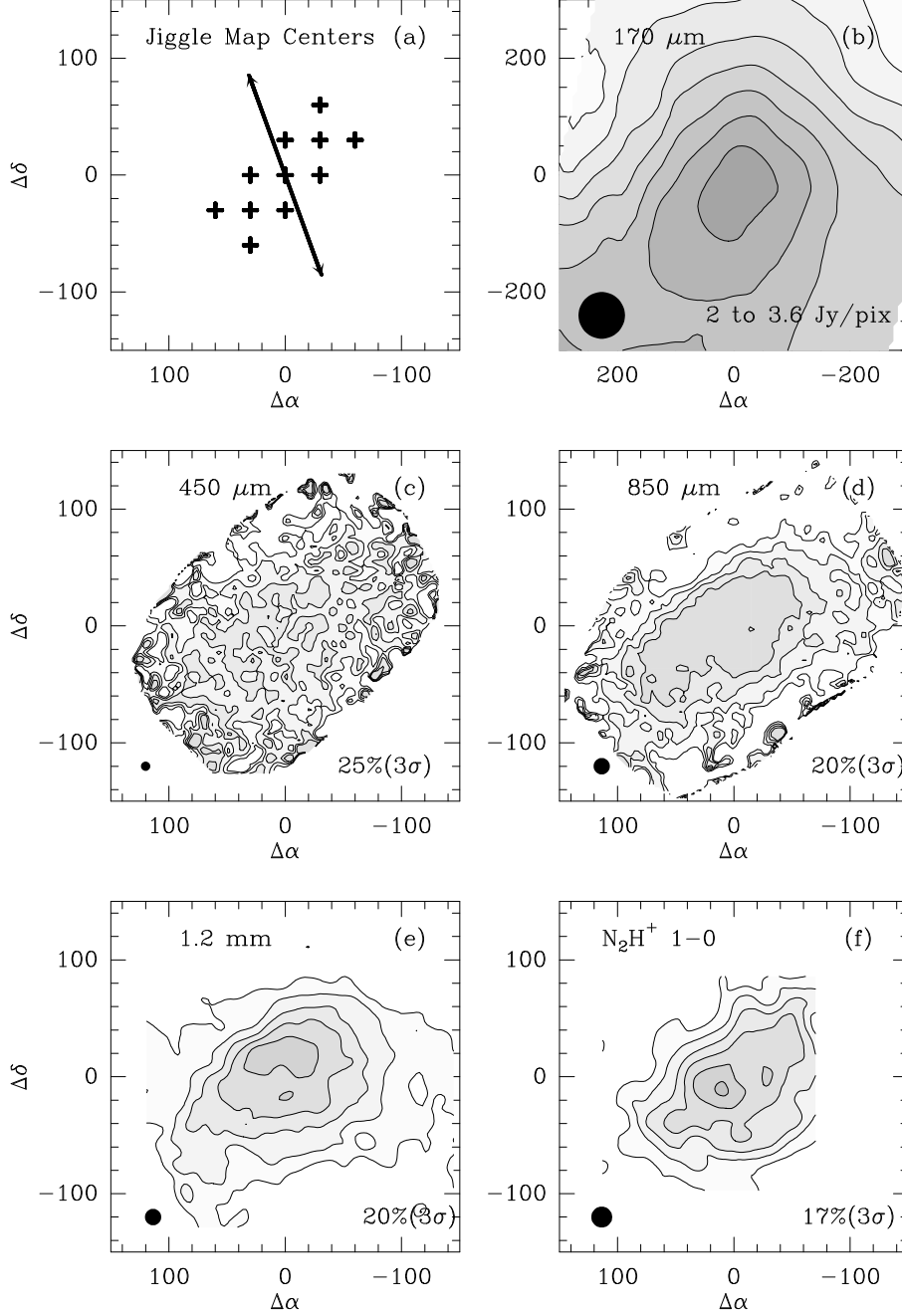


FIG. 1.— The jiggle map pointing centers are plotted with the chop direction (a). The (0,0) position is J2000.0 $\alpha = 4^h 10^m 52.5^s$, $\delta = +25^\circ 9' 55''$. Contour maps of L1498 at 170 μm (b; Ward-Thompson et al. 2002), 450 μm (c), 850 μm (d), 1200 μm (e; Tafalla et al. 2004), and $I(T_A^*)$ of N₂H⁺ $J = 1 \rightarrow 0$ (f). The contour levels are as follows (lowest contour and contour increment in percentage of the peak flux): (N₂H⁺) 17%(3 σ), (1200 μm) 20%(3 σ) increasing by 20% ; (850 μm) 20%(3 σ) increasing by 20% ; (450 μm) 25%(3 σ) increasing by 25% ; and (170 μm) 2.0 to 3.6 Jy/pixel increasing by 0.2 Jy/pixel. **The 170 μm image is plotted on a scale that is twice as large as the other images.**

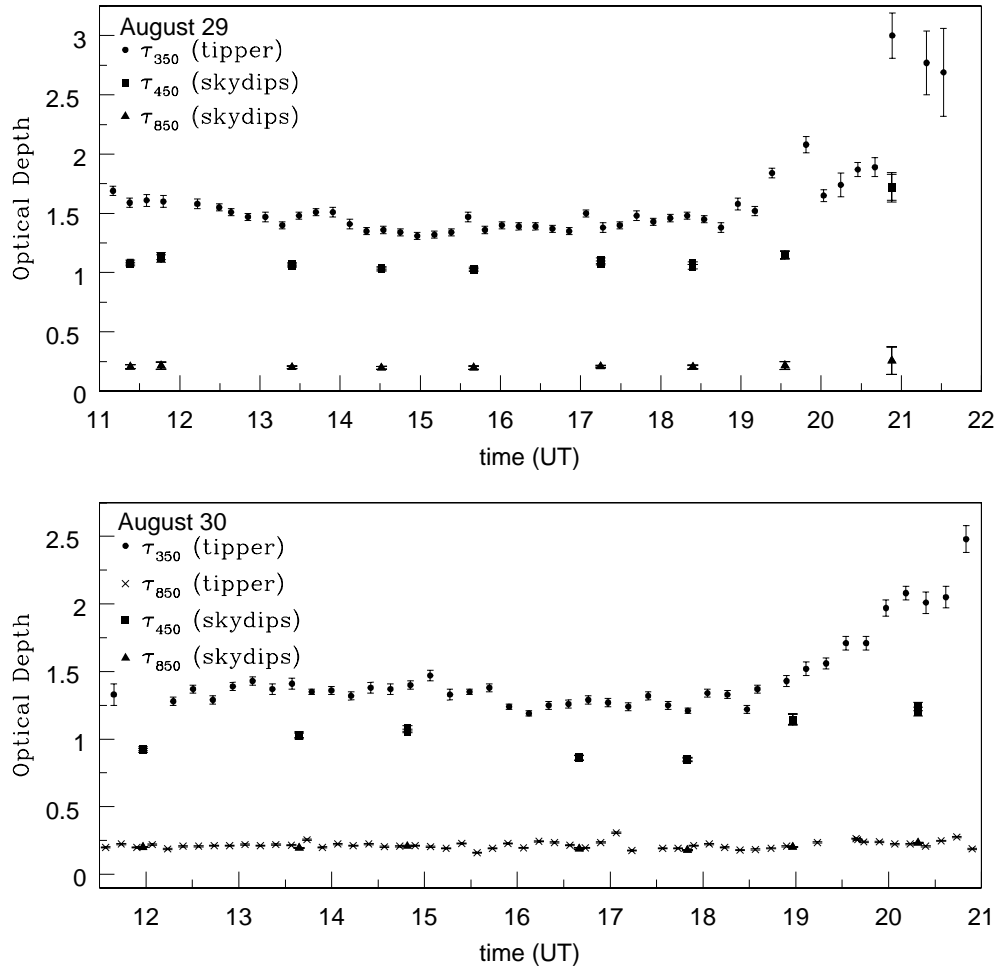


FIG. 2.— Opacity at 350, 450 and 850 μm for August 29 and 30, 1998. The opacity was very stable throughout both nights except for 450 μm observations during the final two hours of the morning shift (after sunrise).

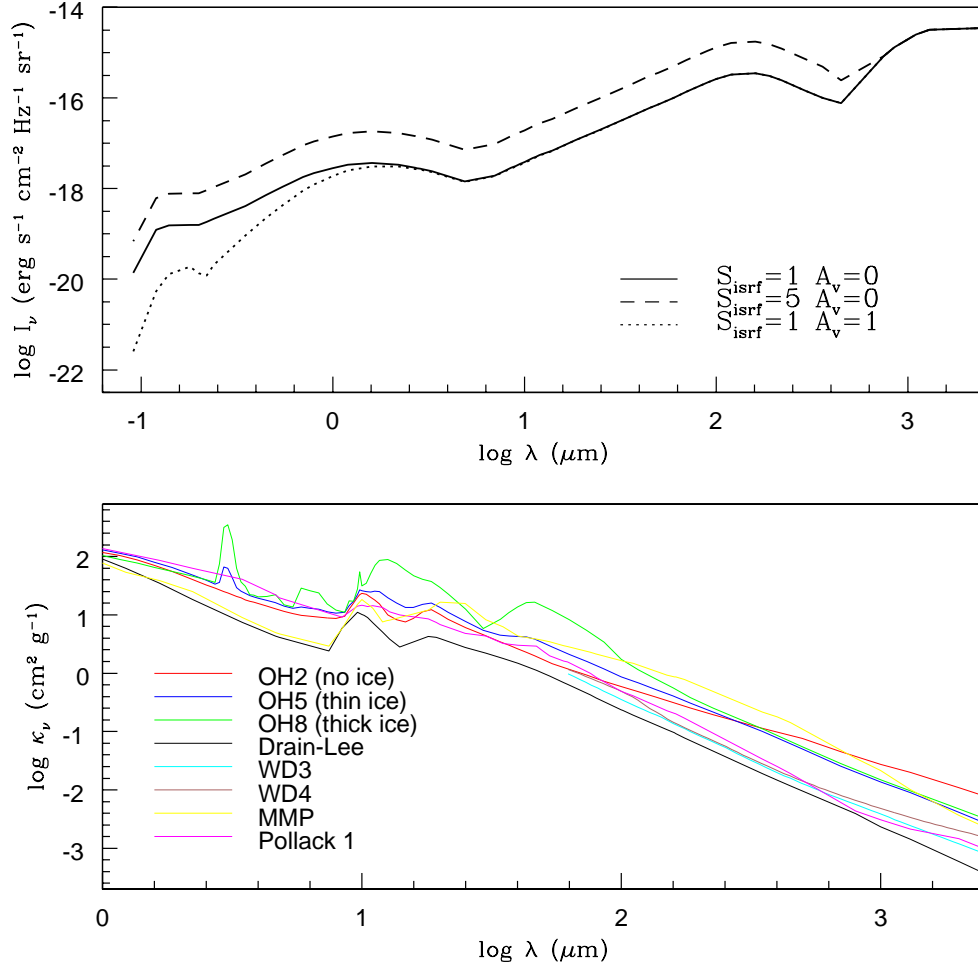


FIG. 3.— The specific intensity of the ISRF with variations in s_{isrf} and A_v (top panel). The dust mass opacities (total gas + dust mass) used in dust models (bottom panel). A $M_{\text{gas}}/M_{\text{dust}} = 100$ was assumed.

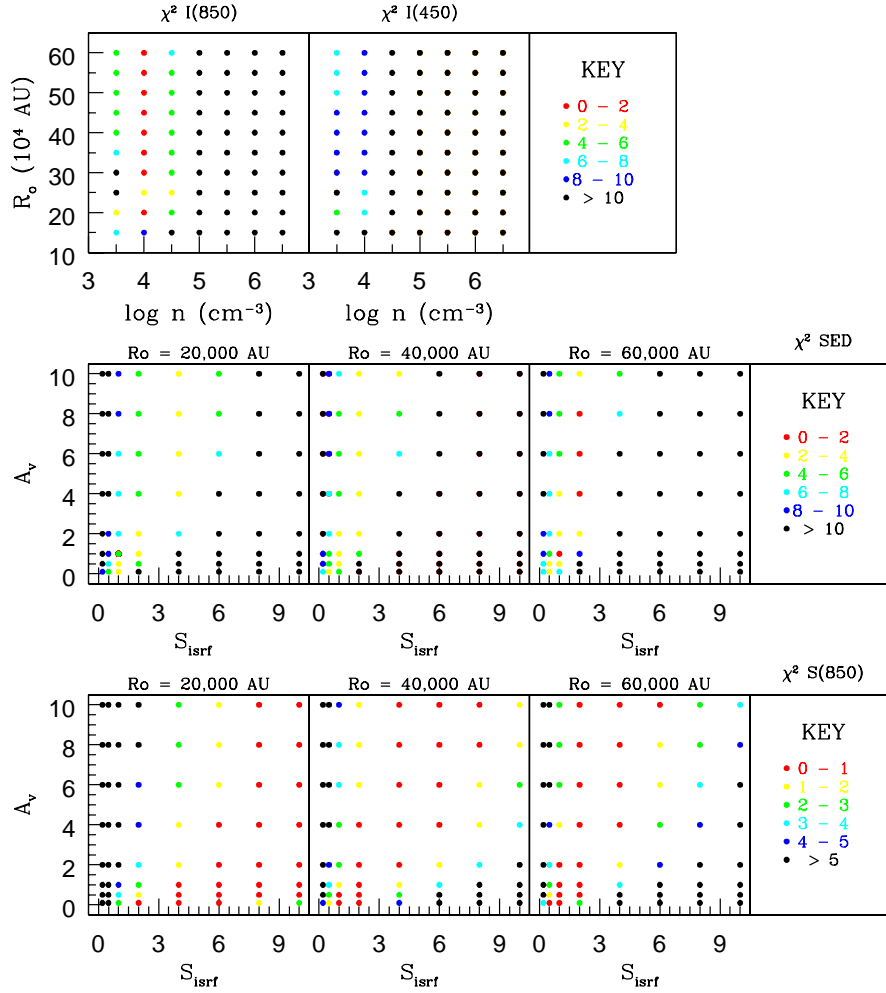


FIG. 4.— Color coded χ^2_r are plotted for the radiative transfer model grid for OH5 dust. $\chi^2(I_{850})$ and $\chi^2(I_{450})$ are plotted for a grid of n_c and R_o (top row). $\chi^2(SED)$ (middle row) and $\chi^2(S_{850})$ (bottom row) are plotted for grids of s_{isrf} and A_v with outer radii of 20,000, 40,000, and 60,000 AU. Note that red points represent the best χ^2_r .

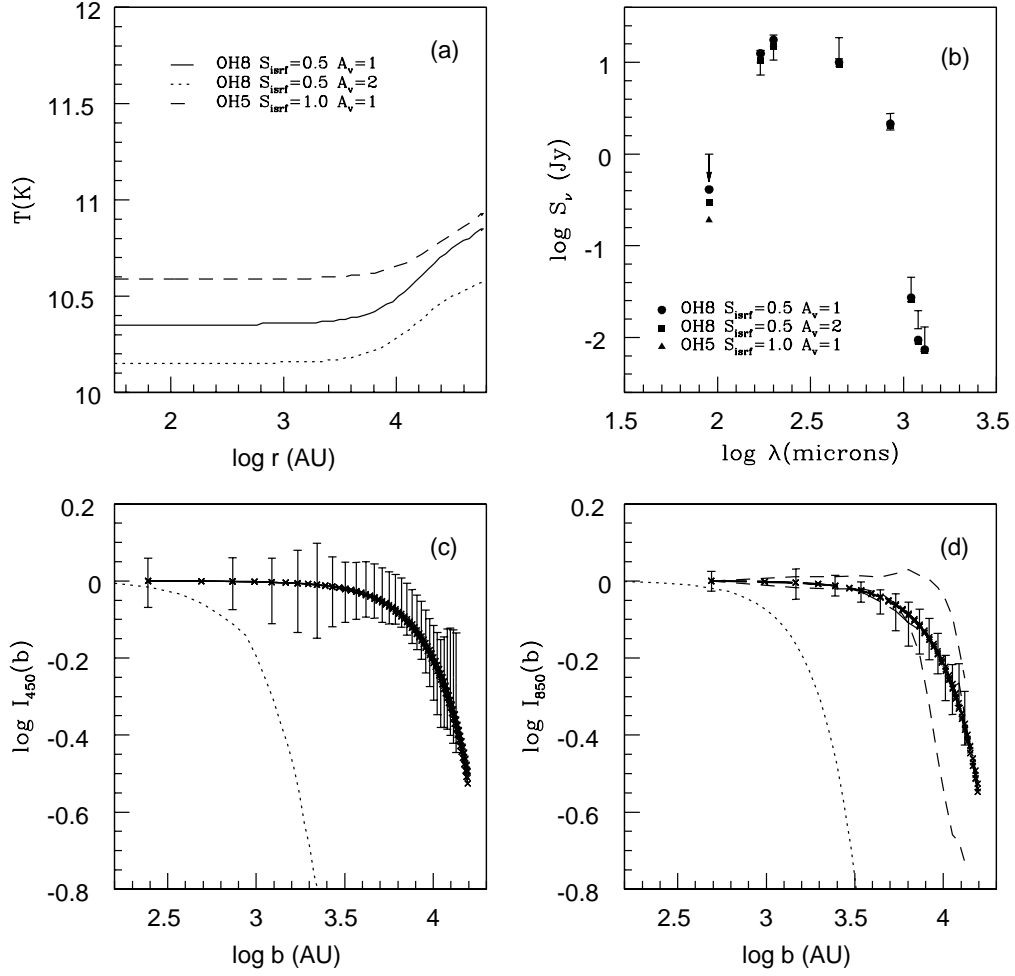


FIG. 5.— Dust temperature profile (panel a), SED (b), $I_{850}(b)$ profile (c), and $I_{450}(b)$ profile (d) for the best fitted models. The Uranus beam profile is shown in the 850 and 450 μm profile. The sector-average radial profiles at 850 μm are plotted as dashed-lines (d).

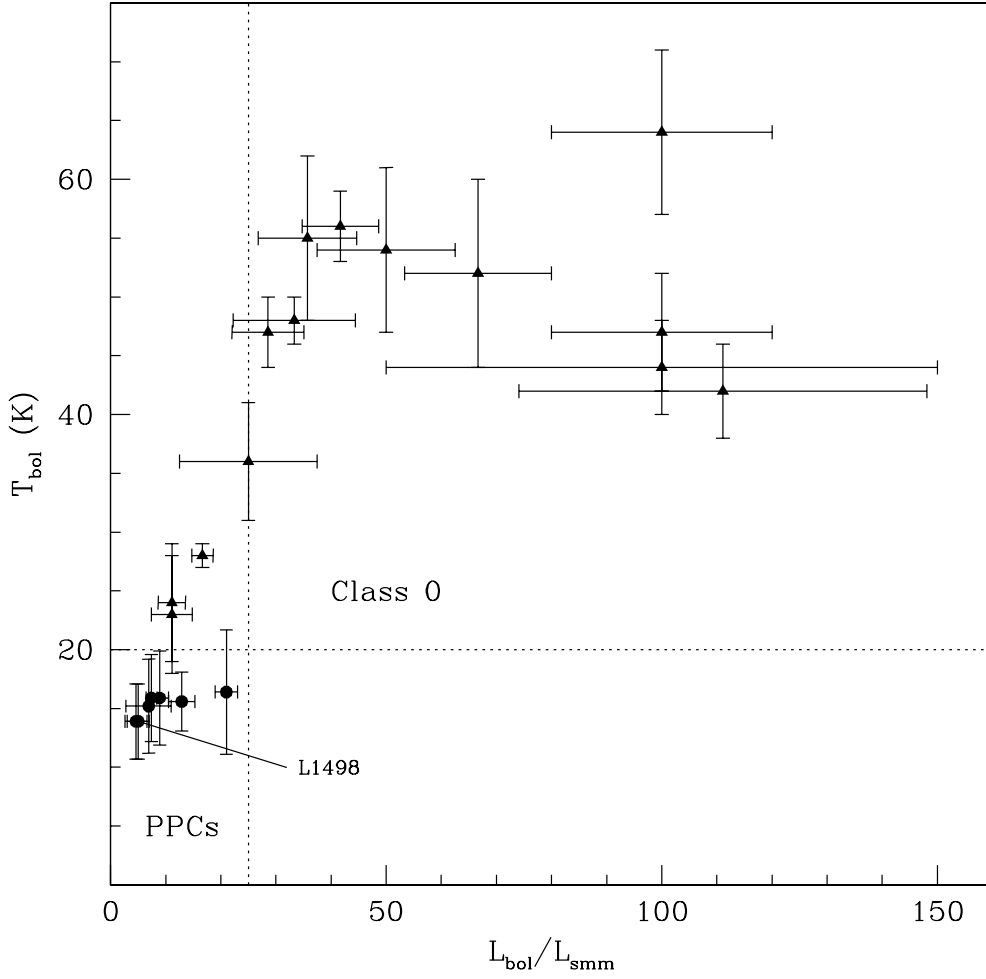


FIG. 6.— The standard evolutionary indicators for low-mass protostars are plotted: T_{bol} vs. $\frac{L_{bol}}{L_{smm}}$. PPCs are plotted as circles and Class 0 sources (Shirley et al. 2000, Young et al. 2003) are plotted as triangles. There is no correlation between these indicators for PPCs; however, all observed PPCs have $T_{bol} < 20$ K and $\frac{L_{bol}}{L_{smm}} < 25$.

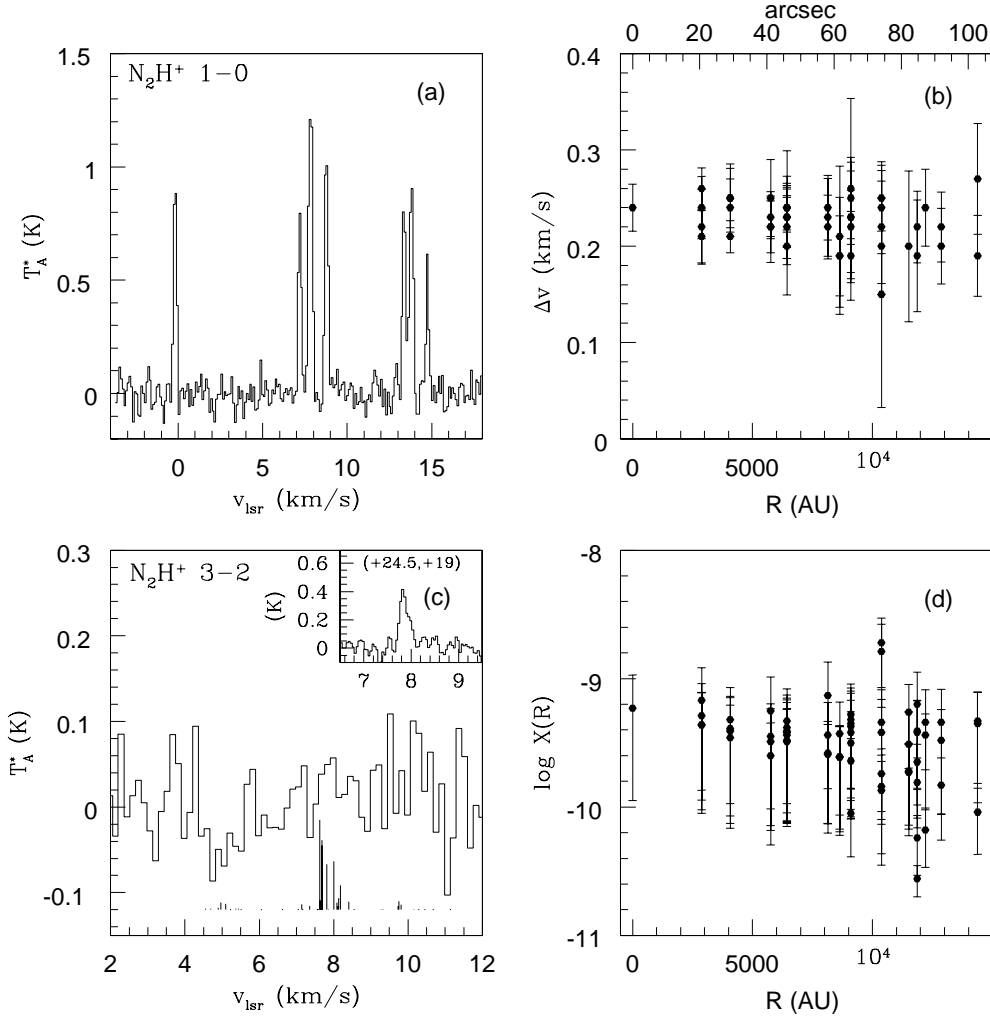


FIG. 7.— The N_2H^+ $J = 1 \rightarrow 0$ spectrum (a) towards the SCUBA continuum centroid (J2000.0 $\alpha = 4^h 10^m 53.3^s$, $\delta = +25^\circ 9' 39''$). The linewidth of the isolated hyperfine component ($JF_1F = 101 \rightarrow 012$) is plotted versus radius (b). The N_2H^+ $J = 3 \rightarrow 2$ spectrum at the SCUBA continuum centroid is shown in panel (c) with a theoretical hyperfine stick spectrum. The N_2H^+ $J = 3 \rightarrow 2$ detection (Crapsi et al. 2004) toward the 1.2 mm continuum peak (J2000.0 $\alpha = 4^h 10^m 51.5^s$, $\delta = +25^\circ 9' 58''$) is shown in the inset (c). The abundance of N_2H^+ versus radius is plotted in panel (d) with statistical errorbars (σ_I , σ_τ , & σ_{S_ν}). No significant variations of the linewidth and abundance are observed on scales out to 15000 AU.

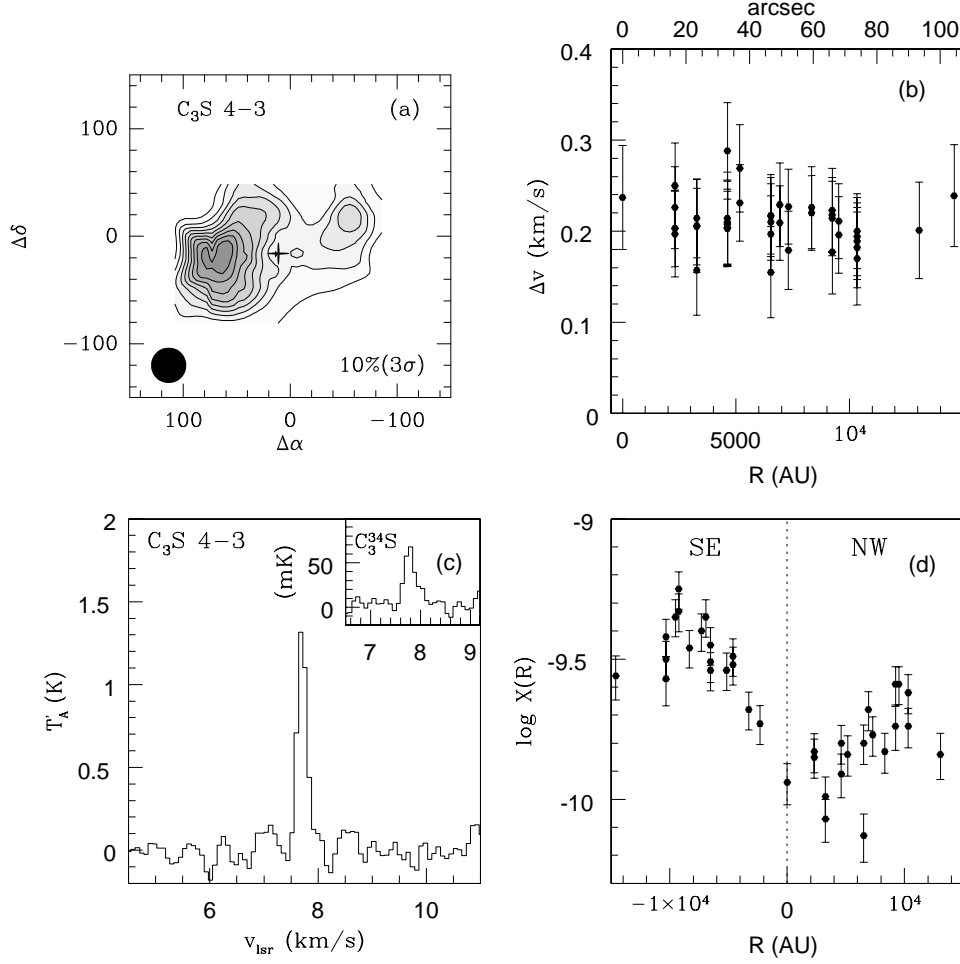


FIG. 8.— The C_3S $J=4 \rightarrow 3$ integrated intensity map is plotted in panel (a) with a cross at the position of the SCUBA dust continuum centroid. The (0,0) position is identical to Figure 1 (J2000.0 $\alpha = 4^h 10^m 52.5^s$, $\delta = +25^\circ 9' 55''$). The variation of linewidth is shown with radius (b). The C_3S and $C_3^{34}S$ (inset) $J=4 \rightarrow 3$ spectra (c) towards the SE C_3S peak (J2000.0 $\alpha = 4^h 10^m 56.9^s$, $\delta = +25^\circ 9' 22.5''$). The abundance of C_3S versus radius in the major axis sector (§2.1.2) is plotted in panel (d) with statistical errorbars (σ_I & σ_{S_ν}). $R=0$ is the dust continuum centroid position; $-R$ refers to positions to the SE. Significant depletion is seen toward the dust continuum centroid.

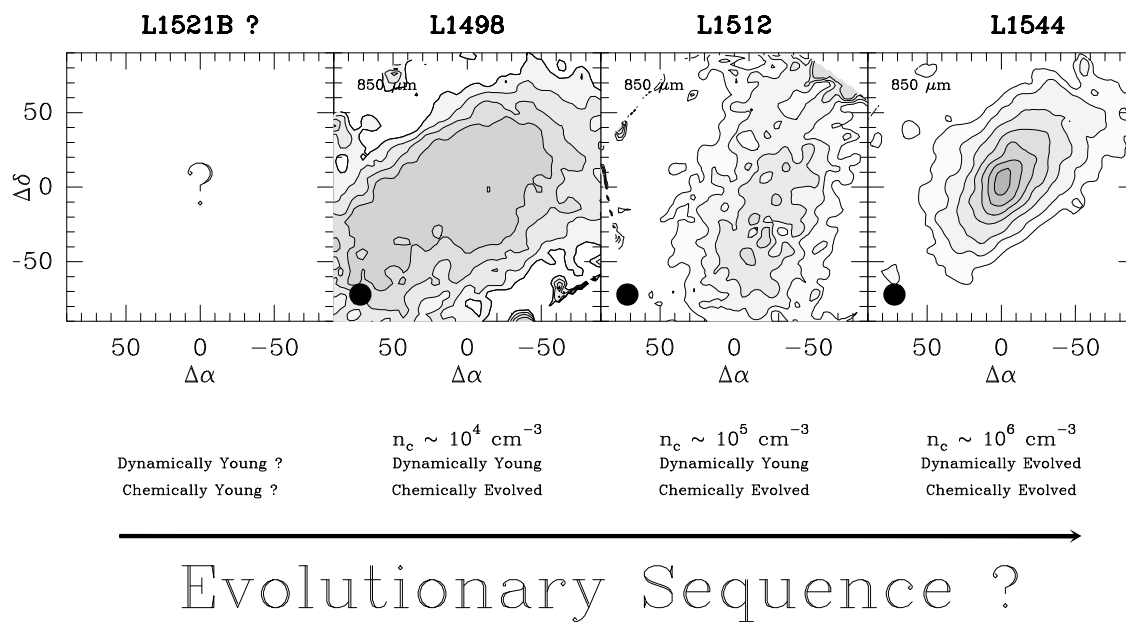


FIG. 9.— Is this a possible evolutionary sequence for PPCs in Taurus-Auriga? The $850 \mu\text{m}$ images of L1512 and L1544 are from Shirley et al. (2000) while the modeled central densities are from Evans et al. (2001). Lee et al. (2003) have characterized the chemical states of L1512 and L1544. There are no published or archive submillimeter detections of the nascent pre-protostellar candidate, L1521B.

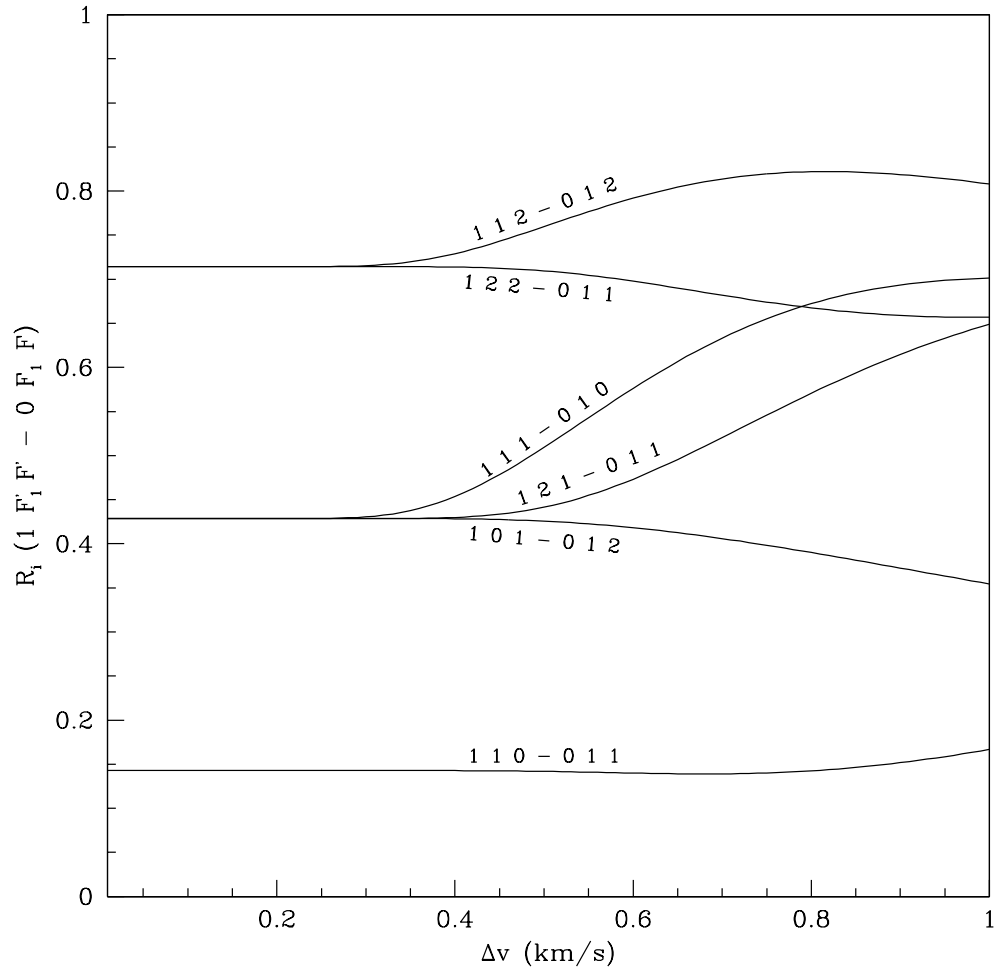


FIG. 10.— The variation of the ratio of relative strengths for $\text{N}_2\text{H}^+ J = 1 \rightarrow 0$ hyperfine lines with linewidth. The theoretical ratios are valid for $\Delta v \leq 0.3 \text{ km/s}$.

TABLE A1
L1498 SPECTRAL ENERGY DISTRIBUTION

λ (μm)	S_ν (Jy)	θ (")	Ref.
90	≤ 1.0	150	1
170	10.4 (...)	150	1 ^a
200	15.2 (...)	150	1 ^a
450	0.700 (0.080)	18	2
450	2.69 (0.59)	40	3
450	14.70 (2.42)	120	3 ^a
800	0.120 (0.018)	18	2
850	0.376 (0.021)	40	3
850	2.30 (0.08)	120	3 ^a
1100	0.035 (0.006)	18	2 ^a
1200	0.016 (0.004)	12	4 ^a
1300	0.010 (0.003)	12	2 ^a

^aFluxes used in calculation of χ^2_{SED} .

References. — 1. Ward-Thompson et al. 2002, 2. Ward-Thompson et al. 1994, 3. This paper, 4. Tafalla et al. 2004

TABLE A2
DUST OPACITY PROPERTIES

Model Name	Description	β_{smm} ^a	$\kappa_\nu(850)$ ($\text{cm}^2 \text{ g}^{-1}$)	Ref.
Draine-Lee	Silicates + Carbonaceous grains	2.0	0.003	1
WD3	Silicate + Carbonaceous + PAH ISM fit	1.8	0.005	2
WD4	Silicate + Carbonaceous + PAH ISM fit	1.6	0.006	2
Pollack1	Silicates + Organic C	2.2	0.004	3
MMP	Empirical Fit to ISM	2.3	0.030	4
OH2	Coagulated for 10^5 yrs. no ice mantles	1.3	0.034	5
OH5	Coagulated for 10^5 yrs. thin ice mantles	1.8	0.018	5
OH8	Coagulated for 10^5 yrs. thick ice mantles	1.9	0.022	5

^a $\kappa \sim \nu^\beta$ where β_{smm} is determined by a linear regression over $\lambda \in [350\mu\text{m}, 1300\mu\text{m}]$.

References. — 1. Draine & Lee 1984, 2. Weingartner & Draine 2001, 3. Pollack et al. 1994, 4. Mathis, Metzger, & Panagia 1983, 5. Ossenkopf & Henning 1994

TABLE A3
BEST-FITTED MODELS^a

$\log n_c$ (cm^{-3})	R_o (10^4 AU)	s_{isrf}	A_V (mag)	κ_ν	$\chi_r^2(I_{850})$	$\chi^2(S_{850})$	$\chi_r^2(SED)$
4.0	60	0.5	1.0 ^b	OH8	0.67	0.12	0.84
4.0	60	2.0	4.0	OH5	0.52	0.10	0.90
4.0	60	2.0	6.0	OH5	0.52	0.26	0.84
4.0	60	0.5	2.0 ^b	OH8	0.66	0.28	0.88
4.0	60	1.0	1.0 ^b	OH5	0.58	0.35	0.90
4.0	60	2.0	8.0	OH5	0.52	0.46	0.97

^aModels for which $\{\chi_r^2(I_{850}) \in [0, 1]\} \cap \{\chi_r^2(S_{850}) \in [0, 1]\} \cap \{\chi_r^2(SED) \in [0, 1]\}$.

^bModel is consistent with Cambr  sy 1999 optical extinction constraint that $A_V \leq 3$ mag.

TABLE A4
PROPERTIES OF NEARBY PPCs OBSERVED WITH ISOPHOT^a AND SCUBA

Source	$\alpha_{J2000.0}$ ^b (^h ^m ^s)	$\delta_{J2000.0}$ ^b ([°] ['] ^{''})	Ref. ^c	D (pc)	$2a \times 2b$ (AU \times AU)	$R_{1/2}$ (AU)	a/b	L_{bol} (L _⊙)	$\frac{L_{bol}}{L_{smm}}$	T_{bol} ^d (K)	$M_D(10.5K)$ ^e (M _⊙)
L1498	04 10 53.3	+25 09 39	1	140	27600×15000	10170	1.8	0.12 (0.02)	5 (2)	13.9 (3.2)	0.67
L1517B	04 55 18.1	+30 37 48	3	140	11600×9700	5300	1.2	0.06 (0.01)	18 (9)	15.2 (3.5)	0.67
L1512	05 04 08.2	+32 43 20	2	140	19000×8500	6350	2.2	0.10 (0.02)	7 (4)	15.2 (4.0)	0.53
L1544	05 04 17.1	+25 10 48	2	140	10900×5700	3940	1.9	0.15 (0.02)	5 (2)	13.9 (3.2)	1.06
L183	15 54 08.5	−02 52 32	3	150	11400×6200	4200	1.8	0.09 (0.01)	13 (3)	15.6 (2.5)	0.89
L1709A	16 30 50.4	−23 42 05	3	125	15800×10500	6440	1.5	0.09 (0.02)	...	15.4 (4.9)	0.98
L1689B	16 34 49.2	−24 38 07	2	125	9600×7700	4300	1.3	0.13 (0.02)	7 (1)	15.9 (3.7)	0.74
L63	16 50 14.4	−18 06 17	3	160	12400×7800	4920	1.6	0.20 (0.04)	21 (2)	16.4 (5.3)	1.15
B68	17 22 39.0	−23 49 57	4	95	9500×7500	5530	1.3	0.05 (0.02)	5 (2)	14.5 (3.5)	0.50
B133	19 06 08.0	−06 52 52	2	200	14900×12100	6710	1.2	0.37 (0.06)	9 (2)	15.9 (4.0)	1.22
$\langle x \rangle$				142		5790	1.6	0.14	9.9	15.2	0.8
$\mu_{1/2}(x)$ ^f				140		5420	1.55	0.11	7.4	15.3	0.9
σ_x				27		1830	0.4	0.09	6.0	0.9	0.3

^aISOPHOT fluxes from Ward-Thompson et al. 2002.

^bSCUBA 850 μ m continuum FWHM contour centroid in J2000.0 coordinates.

^cReference for SCUBA observations.

$$^d T_{bol} = \frac{h\zeta(4)}{4k\zeta(5)} \frac{\int_0^\infty \nu S_\nu d\nu}{\int_0^\infty S_\nu d\nu}.$$

^eDust-determined mass in a 120'' aperture.

^fMedian of the sample.

References. — 1. This paper; 2. Shirley et al. 2000; 3. CADC SCUBA Archive; 4. Bianchi et al. 2003, Lai et al. 2003

TABLE A5
 $\text{N}_2\text{H}^+ J = 1 \rightarrow 0$ HYPERFINE TRANSITIONS

$J'F_1'F' \rightarrow JF_1F$	s_i	$J'F_1'F' \rightarrow JF_1F$ Standard Notation	ν (GHz)	Δv (km/s)	R_i
1 1 0 \rightarrow 0 1 1	$\frac{1}{27}$	1 1 0 \rightarrow 0 1 1	93.1716200	+6.944	$\frac{1}{7}$
1 1 2 \rightarrow 0 1 2	$\frac{5}{36}$	1 1 2 \rightarrow 0 1 2	93.1719168	+5.988	$\frac{5}{7}$
1 1 2 \rightarrow 0 1 1	$\frac{5}{108}$				
1 1 1 \rightarrow 0 1 2	$\frac{5}{108}$				
1 1 1 \rightarrow 0 1 1	$\frac{3}{108}$				
1 1 1 \rightarrow 0 1 0	$\frac{1}{27}$	1 1 1 \rightarrow 0 1 0	93.1720533	+5.549	$\frac{3}{7}$
1 2 2 \rightarrow 0 1 2	$\frac{5}{108}$				
1 2 2 \rightarrow 0 1 1	$\frac{5}{36}$	1 2 2 \rightarrow 0 1 1	93.1734796	+0.956	$\frac{5}{7}$
1 2 3 \rightarrow 0 1 2	$\frac{7}{27}$	1 2 3 \rightarrow 0 1 2	93.1737767	+0.000	1
1 2 1 \rightarrow 0 1 2	$\frac{1}{324}$				
1 2 1 \rightarrow 0 1 1	$\frac{5}{108}$	1 2 1 \rightarrow 0 1 1	93.1739666	-0.611	$\frac{3}{7}$
1 2 1 \rightarrow 0 1 0	$\frac{5}{81}$				
1 0 1 \rightarrow 0 1 2	$\frac{5}{81}$	1 0 1 \rightarrow 0 1 2	93.1762650	-8.011	$\frac{3}{7}$
1 0 1 \rightarrow 0 1 1	$\frac{1}{27}$				
1 0 1 \rightarrow 0 1 0	$\frac{1}{81}$				